Lagrangian statistics in compressible turbulence: Examination of viscous process and invariant dynamics of velocity gradients

Nishant Parashar[1]†, Sawan Suman Sinha [1] and Balaji Srinivasan[2]

[1]Department of Applied Mechanics, Indian Institute of Technology Delhi, New Delhi 110016, India

[2]Department of Mechanical Engineering, Indian Institute of Technology Madras, Chennai 600036, India

(Received xx; revised xx; accepted xx)

1. Introduction

The gradients of the small-scale velocity field and its dynamics in a turbulent flow hold the key to understanding many important nonlinear turbulence processes like cascade, mixing, intermittency and material element deformation. Thus, examination of the velocity gradient tensor in canonical turbulent flow fields have been pursued using experimental measurements (Lüthi *et al.* (2005)), direct numerical simulations (DNS, Ashurst *et al.* (1987*b*)), as well as by employing simpler autonomous dynamical models (ordinary differential equations, Vieillefosse (1982); Cantwell (1992)) of velocity gradients. The pioneering work done by these authors have been further followed up extensively by several researchers for both incompressible (Ashurst *et al.* (1987*b*,*a*); Girimaji (1991); Girimaji & Speziale (1995); Ohkitani (1993); Pumir (1994); da Silva & Pereira (2008); O'Neill & Soria (2005); Chevillard & Meneveau (2006, 2011)) and compressible turbulence (Pirozzoli & Grasso (2004); Suman & Girimaji (2009, 2010*b*, 2012); Danish *et al.* (2016*a*); Parashar *et al.* (2017*a*)). These efforts have led to an improved understanding of small-scale turbulence.

Most DNS or experiment-based studies of fluid mechanics have so far been performed using one-time Eulerian flow field. However, it is desirable to investigate the flow statistics following individual fluid particles (the Lagrangian tracking). Such an investigation is especially required from the point of view of developing/improving simple dynamical models of the velocity gradient dynamics like the restricted Euler equation (REE) (Cantwell (1992); Girimaji & Speziale (1995); Meneveau (2011)) and the enhanced homogenized Euler equation model of Suman & Girimaji (2009). Such simple models, in turn, can be used for closure of Lagrangian PDF method of turbulence (Pope (2002)). An apt example of how Lagrangian statistics can reveal more profound insights into velocity gradient dynamics is the recent experimental study of Xu *et al.* (2011), wherein the authors provided evidence of the so-called "Pirouette effect". Even though the vorticity vector had always been expected to align with the largest strain-rate eigenvector, Eulerian investigations invariably revealed a counterintuitive picture of vorticity aligning most strongly with the intermediate eigenvector of the instantaneous local strain-rate tensor. Xu *et al.* (2011), with their experimental Lagrangian investigations, provided first-hand evidence that indeed the vorticity vector dynamically attempts to align with the largest strain-rate eigenvector at an initial reference time in order to cause intense vortex

† Email address for correspondence: nishantparashar14@gmail.com

stretching, and the alignment tendency as shown by the Eulerian one time field (with the instantaneous intermediate eigenvector) was merely a transient incidental event.

In incompressible flows, Lagrangian studies using the direct numerical simulation of decaying turbulence have earlier been performed by Yeung & Pope (1989), though the authors' focus was on Lagrangian statistics of velocity, acceleration, and dissipation. Recently, Xu *et al.* (2011) have complemented their experimental observations of vorticity alignment with the Lagrangian data extracted from DNS of forced isotropic turbulence. Chevillard & Meneveau (2011) evaluated the Lagrangian model for velocity gradient tensor in its capability to predict vorticity alignment using Lagrangian data obtained from DNS of forced isotropic turbulent flow. Bhatnagar *et al.* (2016) quantified the persistence time of fluid particles in vorticity-dominated and strain-dominated topologies using Lagrangian data obtained from DNS of isotropic forced incompressible turbulence. In compressible turbulence, Lagrangian statistics of velocity gradients have been recently studied by Danish *et al.* (2016*a*) and Parashar *et al.* (2017*a*). While Danish *et al.* (2016*a*) provided the first glimpse of compressibility effects on the alignment tendencies of the vorticity vector, Parashar *et al.* (2017*a*) followed it up and made attempts at explaining the observed behaviour in terms of the dynamics of the inertia tensor of fluid particles and conservation of angular momentum of tetrads representing the fluid particles. In continuation of our effort to develop deeper insight into the dynamics of small-scale turbulence from a Lagrangian perspective, in this work, we focus on another two important aspects of velocity gradient dynamics: (i) evolution of the deformation gradient tensor, (ii) dynamics of flow field topology in compressible turbulence.

Our primary motivation behind investigating the dynamics of the deformation gradient tensor is that this quantity has been used in modeling the viscous processes in both restricted Euler equation (REE) by Jeong & Girimaji (2003). The authors modelled the viscous process using gradient-deformation hypothesis-like assumption, wherein the diffusion is allowed to be amplified as function of the deformation gradient tensor. This model was called the linear Lagrangian diffusion model (LLDM). Later the same model was used by Suman & Girimaji (2009) in their enhanced homogenized Euler equation (EHEE) model. While the REE is the simple dynamical representation of velocity gradient dynamics in incompressible flows, the EHEE model is the counterpart for compressible flows. Even though the EHEE model employing the LLDM approach does capture various Mach number and Prandtl number effects, further improvements are indeed desirable (Danish *et al.* (2014)). From this point of view, in the first part of this work, we subject the LLDM modeling approach to a direct scrutiny by comparing its Lagrangian evolution history against that of the exact process it represents−an examination that has not been previously attempted neither in incompressible nor in compressible turbulence. Direct numerical simulation data of decaying compressible turbulence over a wide range of Mach number along with a well-validated Lagrangian particle tracker is employed for the purpose. Further, the influence of compressibility−parameterized in terms of Mach number, dilatation rate, and topology is also investigated.

In the second part of this work, we examine the evolution of topology itself in compressible turbulence following the Lagrangian trajectories of the invariants of the velocity gradient tensors. The local topology of a compressible flow field depends on the local state of the velocity gradient tensor. Topology can also be visualized as the local streamline pattern as observed with respect to a reference frame which is translating with the centre of mass of a local fluid particle (Chong *et al.* (1990)). Topology actually depends on the nature of eigenvalues of the velocity gradient tensor, and can also be readily determined by knowing the three invariants of the velocity gradient tensor (Cantwell & Coles 1983; Chong *et al.* 1990). Topology can not only be used for

visualization of a flow field; it has been observed to reveal deeper insights into various nonlinear turbulence processes as well (Cantwell (1993); Soria *et al.* (1994)). Recently, Danish *et al.* (2016*b*) have also attempted developing models for scalar mixing using topology as conditioning parameter.

Traditionally, due to the prohibitive demand of computational resources, dynamics of topology have been studied employing an approximate surrogate method called the conditional mean trajectory (CMT). The idea of CMT was proposed by Martín *et al.* (1998). The authors employed merely one-time velocity gradient data of the entire flow field and computed bin-averaged rates-of-change of second and third invariants using the right-hand-side of evolution equations of the invariants. These bin-averaged rates of change conditioned upon their locations were subsequently used to plot trajectories in the Q-R space. The authors called these trajectories as conditional mean trajectories (CMT) and used them as a surrogate approach to study invariant dynamics. Several authors have employed the CMTs to investigate various aspects of dynamic of topology both for incompressible (Ooi *et al.* (1999); Meneveau (2011); Atkinson *et al.* (2012)) and compressible flows (Chu & Lu (2013); Bechlars & Sandberg (2017)). Indeed the work done by previous researchers employing the approximate approach of CMTs have improved our understanding of the distribution and dynamics of topology in compressible turbulence. Even though CMTs provide useful information about dynamics of invariants, they are after all an approximation and merely a surrogate approach in the absence of adequate computational resources (Martín *et al.* (1998)). An investigation of the Lagrangian dynamics in compressible turbulence must be performed if adequate computational resources are available. Indeed such an investigation of invariants using Lagrangian trajectories have been recently performed by Bhatnagar *et al.* (2016) for incompressible turbulence. Thus, we identify the following objectives for the second part of this work: (i) identifying and understanding the differences, if any, between CMT and the Lagrangian trajectory (LT) in compressible turbulence, and (ii) employing the LTs to investigate lifetime of topologies and their interconversion processes.

To address the identified objectives of both parts of this paper, we employ direct numerical simulations of decaying isotropic compressible turbulence and over a wide range of turbulent Mach number (0.6, 1.5) and a moderate range of Reynolds number (70, 350). The Lagrangian dynamics are obtained using an almost time continuous set of flow field along with spline-aided Lagrangian particle tracker (more details in §4).

This paper is organized into seven sections. In §2 we present the governing equations. In §3 we provide details of our direct numerical simulations and the Lagrangian particle tracker. In §4 we explain our study plan. In §5 we evaluate the LLDM model of Jeong & Girimaji (2003) in terms of its ability to mimic the exact viscous diffusion process. In §6 we study the dynamics of topology, compare CMT and LT and quantify lifetime of various flow-topologies existing in compressible turbulence. Section 7 concludes the paper with a summary.

2. Governing Equations

The governing equations of compressible flow field of a perfect gas are the continuity, momentum, energy and state equations:

$$\frac{\partial \rho}{\partial t} + V_k \frac{\partial \rho}{\partial x_k} = - \rho \frac{\partial V_k}{\partial x_k}; \tag{2.1}$$

$$\frac{\partial V_i}{\partial t} + V_k \frac{\partial V_i}{\partial x_k} = - \frac{1}{\rho}\frac{\partial p}{\partial x_i} + \frac{1}{\rho}\frac{\partial \sigma_{ik}}{\partial x_k}, \tag{2.2}$$

$$\frac{\partial T}{\partial t} + V_k \frac{\partial T}{\partial x_k} = - T(n-1)\frac{\partial V_i}{\partial x_i} - \frac{n-1}{\rho R}\frac{\partial q_k}{\partial x_k} + \frac{n-1}{\rho R}\frac{\partial}{\partial x_j}\left(V_i \sigma_{ji}\right), \tag{2.3}$$

$$p = \rho R T, \tag{2.4}$$

where V_i, x_i, ρ, p, T, R, σ_{ik}, q_k, n denote velocity, position, density, pressure, temperature, gas constant, stress tensor, heat flux and ratio of specific heat values, respectively. The quantities σ_{ij} and q_k obey the following constitutive relationships:

$$\sigma_{ij} = \mu\left(\frac{\partial V_i}{\partial x_j} + \frac{\partial V_j}{\partial x_i}\right) + \delta_{ij}\lambda\frac{\partial V_k}{\partial x_k}; \tag{2.5}$$

$$q_k = -K\frac{\partial T}{\partial x_k}, \tag{2.6}$$

where δ_{ij} is the Kronecker delta, K represents the thermal conductivity, and μ and λ denote the first and second coefficients of viscosity respectively ($\lambda = -\frac{2\mu}{3}$) .

The velocity gradient tensor is defined as:

$$A_{ij} \equiv \frac{\partial V_i}{\partial x_j}.$$

The evolution equation of A_{ij} can be obtained by taking the gradient of momentum equation 2.2, as

$$\frac{DA_{ij}}{Dt} = -A_{ik}A_{kj} - \underbrace{\frac{\partial}{\partial x_j}\left(\frac{1}{\rho}\frac{\partial p}{\partial x_i}\right)}_{\mathbb{P}_{ij}} + \underbrace{\frac{\partial}{\partial x_j}\left\{\frac{1}{\rho}\frac{\partial}{\partial x_k}\left[\mu\left(\frac{\partial V_i}{\partial x_k} + \frac{\partial V_k}{\partial x_i} - \frac{2}{3}\frac{\partial V_p}{\partial x_p}\delta_{ik}\right)\right]\right\}}_{\Upsilon_{ij}}, \tag{2.7}$$

where, the operator $\frac{D}{Dt}(\equiv \frac{\partial}{\partial t} + V_k\frac{\partial}{\partial x_k})$ stands for the substantial derivative, which represents the rate of change following a fluid particle. In equation 2.7, the first term on its right-hand side (RHS) represents the self-deformation process of velocity-gradients. The term $\mathbb{P}_{ij}$ is called the pressure Hessian tensor, whereas Υ_{ij} represents the action of viscosity on the evolution of the velocity gradient tensor.

3. Direct numerical simulations and particle tracking

In this work dynamics of invariants of the velocity gradient tensor (VGT) are studied using the direct numerical simulation (DNS) of decaying turbulent flows. Our simulations are performed using the gas kinetic method (GKM). The gas kinetic method (GKM) was originally developed by Xu *et al.* (1996) has been shown to be quite robust in terms of numerical stability and has the ability to capture shock without numerical oscillations for simulating compressible turbulence (Kerimo & Girimaji 2007; Liao *et al.* 2009; Kumar *et al.* 2013; Parashar *et al.* 2017*b*). Our computational domain is of size 2π with a uniform grid and periodic boundary conditions imposed on opposite sides of the domain.

The initial velocity field is generated at random with zero mean and having the following energy spectrum $E(\kappa)$:

$$E(\kappa) = A_0\kappa^4 \exp\left(-2\kappa^2/\kappa_0^2\right), \tag{3.1}$$

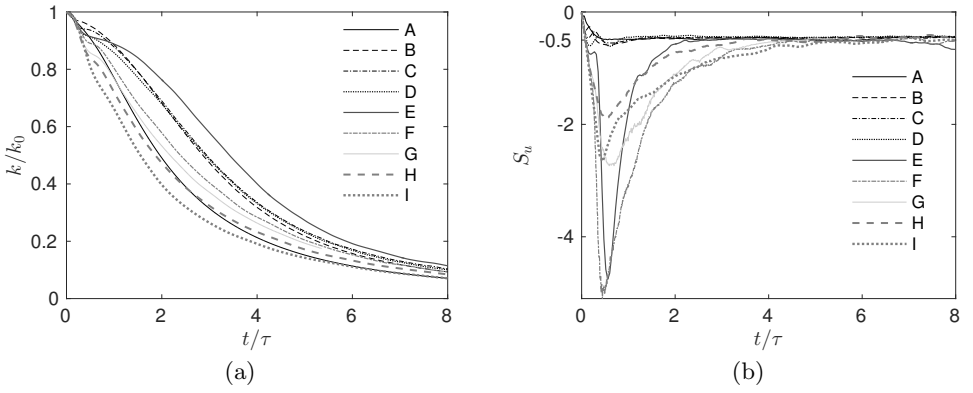

FIGURE 1. Evolution of (a) normalized turbulent kinetic energy $\frac{k}{k_0}$ and (b) Velocity derivative skewness S_u, in Simulations A-G: (Table 1).

where κ is wavenumber. Values for spectrum constants A_0 and κ_0 are provided in Table 1 for various simulations employed in this work. The relevant Reynolds number for isotropic turbulence is the one based on Taylor micro-scale (Re_λ):

$$Re_\lambda = \sqrt{\frac{20}{3\epsilon\nu}}k, \tag{3.2}$$

where k, ϵ, and ν represent turbulent kinetic energy, its dissipation-rate, and kinematic viscosity. For compressible isotropic turbulence, the relevant Mach number is the turbulent Mach number (M_t):

$$M_t = \sqrt{\frac{2k}{nR\overline{T}}}, \tag{3.3}$$

where $\overline{T}$ represents mean temperature. Following the work of Kumar *et al.* (2013), we have used 4^{th} order accurate weighted-essentially-non-oscillatory (WENO) method for interpolation of flow variables, in-order to simulate high Mach number compressible turbulent flows. Our solver has been extensively validated with established DNS results of compressible turbulent flows (Danish *et al.* (2016*a*)). In total, this study employs seven different simulations (Simulations A-G). Descriptions of these simulations are presented in Table 1.

In Figure 1(a) we present evolution of turbulent kinetic energy (k) observed in Simulations A-G. In Figure 1(b), we present the evolution of skewness of the velocity derivative (S_V) defined as:

$$k = \frac{1}{2}\overline{V_i V_i}; \tag{3.4}$$

$$S_{V_i} = \frac{\overline{\left(\frac{\partial V_i}{\partial x_i}\right)^3}}{\left[\left(\frac{\partial V_i}{\partial x_i}\right)^2\right]^{3/2}}, \tag{3.5}$$

$$S_V = \frac{S_{V_1} + S_{V_2} + S_{V_3}}{3}. \tag{3.6}$$

Note that the time has been normalized using τ, which represents eddy turnover time (Yeung & Pope 1989; Elghobashi & Truesdell 1992; Samtaney *et al.* 2001; Martín *et al.*

Simulation	Re_λ	M_t	Grid size	A_0	κ_0
A.	70	0.075	128^3	0.000023	4
B.	350	0.6	1024^3	0.0015	4
C.	150	1.0	512^3	0.0042	4
D.	100	1.0	512^3	0.0042	4
E.	70	1.0	256^3	0.0042	4
F.	70	1.25	256^3	——	4
G.	70	1.5	256^3	0.0094	4

TABLE 1. Initial parameters of DNS simulations.

2006):

$$\tau = \frac{\lambda_0}{u_0'}; \tag{3.7}$$

where u_0' and λ_0 are the root mean square (rms) velocity and integral-length-scale of the initial flow field (at time, $t = 0$).

To extract Lagrangian statistics, a Lagrangian particle tracker (LPT) is used to extract the full time-history of tagged fluid particles. Our LPT obtains the trajectory ($\mathbf{X}^+(\mathbf{y}, \mathbf{t})$) of a fluid particle by solving the following equation of motion:

$$\frac{\partial \mathbf{X}^+(t, \mathbf{y})}{\partial t} = \mathbf{V}\left(\mathbf{X}^+(t, \mathbf{y}), t\right), \tag{3.8}$$

where the superscript "+" represents a Lagrangian flow variable, and $\mathbf{y}$ indicates the label/identifier assigned to the fluid particle at a reference time (t_{ref}). The initial value of $\mathbf{X}^+$ at a reference time is chosen at random. Using this initial condition, we then integrate Equation 3.8 by employing second order Runge-Kutta method. However, upon integration, the position of the fluid particle at a subsequent time instant may not fall exactly on one of the grid points of computational domain used in the parent DNS. Therefore, an interpolation method is required to find relevant flow quantities at the particle's subsequent locations. Following the work of Yeung & Pope (1988), we choose cubic spline interpolation for this purpose. Like our DNS solvers, our LPT algorithm and implementation have been adequately validated. Details are available in Danish *et al.* (2016*a*).

4. Plan of study

In this section we present our plan of study and also explain the quantities that are employed to perform the desired investigations. In §4.1 we present the study plan for the first part of the work, where we examine the Lagrangian dynamics of the deformation gradient tensor. In §4.2 we explain our study plan for the second part of this work, which involves comparing CMT and LT and consequently using these trajectories to investigate interconversion processes of topologies existing in compressible turbulence.

4.1. *Study I*

In the first part of this work we focus on the viscous process Υ in the evolution equation of the velocity gradient (Equation 2.7):

$$\Upsilon_{ij} = \underbrace{\nu \frac{\partial A_{ij}}{\partial x_k \partial x_k}}_{\Upsilon_{I_{ij}}} + \underbrace{\nu \frac{\partial A_{kk}}{\partial x_i \partial x_j}}_{\Upsilon_{II_{ij}}} - \underbrace{\frac{\nu}{\rho}\frac{\partial \rho}{\partial x_j}\left(\frac{\partial A_{ik}}{\partial x_k} + \frac{1}{3}\frac{\partial A_{kk}}{\partial x_i}\right)}_{\Upsilon_{III_{ij}}}. \tag{4.1}$$

In Equation 4.1, $\Upsilon_{I_{ij}}$ and $\Upsilon_{II_{ij}}$ are essentially the diffusion terms and $\Upsilon_{III_{ij}}$ is an interaction between density gradient and viscous process of the A_{ij} tensor. From the point of view of a dynamical equation of A_{ij} (like REE of Vieillefosse (1982) and HEE of Suman & Girimaji (2009)), each of the three viscous terms ($\Upsilon_{I_{ij}}$, $\Upsilon_{II_{ij}}$ and $\Upsilon_{III_{ij}}$) represents a non-local, unclosed process. Jeong & Girimaji (2003) proposed a model for the first term $\Upsilon_{I_{ij}}$. This model is called the linear Lagrangian diffusion model (LLDM). The LLDM model approximates the viscous diffusion term $\Upsilon_{I_{ij}}$ as:

$$\nu \frac{\partial A_{ij}}{\partial x_k \partial x_k} \approx \frac{C_{kk}^{-1}}{3\tau_\nu} A_{ij}, \tag{4.2}$$

where, C_{ij} represents the right Cauchy Green tensor, which is derived from the deformation gradient tensor D_{ij}:

$$D_{ij} \equiv \frac{\partial x_i}{\partial X_j}; \tag{4.3}$$

$$C_{ij} \equiv D_{ki} D_{kj}. \tag{4.4}$$

Here, x_i is the Eulerian position vector of the particle at time t, initially located at position vector X_j at time t_{ref}. τ_ν is a molecular viscous relaxation time scale (Jeong & Girimaji 2003) .

Suman & Girimaji (2009) have employed the same LLDM model for the closure of their enhanced homogenized Euler equation model (EHEE). Even though the LLDM achieves a mathematically closed form, in this work, we intend to perform direct scrutiny of this model using our DNS results. Such an investigation is required for a deeper understanding of the model and may lead to further improvement in its performance.

Our interest is to examine how the viscous process Υ undergoes changes in comparison to its state at a reference time following a fluid particle. For monitoring this change we define an amplification ratio $r(t, t_{ref}$, which is defined as:

$$r(t, t_{ref}) = \frac{\sqrt{\Upsilon_{ij}(t)\Upsilon_{ij}(t)}}{\sqrt{\Upsilon_{ij}(t_{ref})\Upsilon_{ij}(t_{ref})}}, \tag{4.5}$$

where, $\Upsilon_{ij}(t)$ and $\Upsilon_{ij}(t_{ref})$ are values of the quantity Υ_{ij} associated with an identified fluid particle at an arbitrary time t and at a reference time t_{ref} respectively. Since an individual particle represents just one realization, we obtain a relevant statistics by calculating the mean of $r(t, t_{ref})$ over several identified fluid particles of a homogeneous flow field. The resulting quantity is referred as $\langle r(t, t_{ref})\rangle$, and is truly a two-time Lagrangian correlation.

Direct numerical simulation of compressible decaying turbulence along with our Lagrangian particle tracker (LPT) are employed to access $\langle r(t, t_{ref})\rangle$. A set of 1,000,000 particles are identified at t_{ref} for the purpose. Further, to identify the role of turbulent Mach number (M_t), normalized dilatation (a_{ii}) and topology ($\mathcal{T}$), we also calculate $\langle r(t, tref)\rangle$ conditioned upon selected particles with a specified M_t, or a_{ii} or $\mathcal{T}$ at t_{ref}. These conditional statistics are symbolically represented as $\langle r(t, t_{ref})|M_t\rangle$, $\langle r(t, t_{ref})|a_{ii}\rangle$

and $\langle r(t,t_{ref})|\mathcal{T}\rangle$ respectively. Direct numerical simulations with a range of M_t and Re_λ are employed for our work. The relevant results and discussion are presented in §5.

The normalized dilatation rate, which is used as a conditioning parameter, is the trace of the normalized velocity gradient tensor, defined as:

$$a_{ij} = A_{ij}/\sqrt{A_{mn}A_{mn}}. \tag{4.6}$$

The normalized dilatation-rate of a fluid particle (henceforth, referred to as just "dilatation") represents the normalized rate of change in density of a local fluid particle:

$$\frac{1}{\rho}\frac{d\rho}{dt'} = -a_{ii} \tag{4.7}$$

where $dt' = dt\sqrt{A_{ij}A_{ij}}$ represents time normalized with the local magnitude of the velocity gradient tensor itself. A positive value of a_{ii} implies an expanding fluid element, a negative value of a_{ii} implies a contracting fluid element. A fluid particle with instantaneous $a_{ii} = 0$ implies a volume preserving fluid element.

Direct numerical simulations with a range of initial M_t and Re_λ are employed for studying the behaviour of $\langle r(t,t_{ref})\rangle$, we examine the behaviour of viscous process modelled using the LLDM model.

?????????????????????????? ??????????????????????????
??
??

We define another ratio $r_m(t,t_{ref})$:

$$r_m(t,t_{ref}) = \frac{\sqrt{C_{kk}^{-1}(t)\sqrt{A_{ij}(t)A_{ij}(t)}}}{\sqrt{C_{kk}^{-1}(t_{ref})\sqrt{A_{ij}(t_{ref})A_{ij}(t_{ref})}}}, \tag{4.8}$$

where, $\sqrt{C_{kk}^{-1}(t)\sqrt{A_{ij}(t)A_{ij}(t)}}$ and $\sqrt{C_{kk}^{-1}(t_{ref})\sqrt{A_{ij}(t_{ref})A_{ij}(t_{ref})}}$ represents quantities associated with an identified fluid particle at t and t_{ref} respectively. Similar to $r(t,t_{ref})$, $r_m(t,t_{ref})$ is also accessible uing our DNS database and the Lagrangian particle tracker. The corresponding mean calculated using the same set of 1,000,000 particles as before, leads to the Lagrangian statistics:

$$\langle r_m(t,t_{ref})\rangle = \left\langle \frac{\sqrt{C_{kk}^{-1}(t)\sqrt{A_{ij}A_{ij}(t)}}}{\sqrt{C_{kk}^{-1}(t_{ref})\sqrt{A_{ij}A_{ij}(t_{ref})}}} \right\rangle. \tag{4.9}$$

Note that in the LLDM model of Jeong & Girimaji (2003) τ_ν represents a laminar viscous time scale. Even though we do not have a direct estimate of this quantity for our DNS set-up of compressible decaying turbulence, it has no net contribution to $\langle r_m(t,t_{ref})\rangle$. The evolution of $\langle r_m(t,t_{ref})\rangle$ is examined and careful comparisons of this quantity is made against the behaviour of $\langle r(t,t_{ref})\rangle$ in §5.2.

4.2. *Study II*

In this second part of this study, we focus on the dynamics of the topology of compressible turbulence.

The topology of a fluid particle is the local streamline pattern as observed with respect to a reference frame which is translating with the center of mass of the fluid particle. The topology of a fluid particle depends on the nature of eigenvalues of the velocity gradient tensor. However, it can also be inferred with the knowledge of the three invariants of the

Acronyms	$p=0$	$p<0$	$p>0$	Eigenvalues of a_{ij}
SFS	$r<0$	$r<0$ & $S2>0$	$r<0$	complex
UFC	$r>0$	$r>0$	$r>0$ & $S2<0$	complex
UNSS	$r>0$ & $q<0$	$r>0$	$r>0$ & $q<0$	real
SNSS	$r<0$ & $q<0$	$r<0$ & $q<0$	$r<0$	real
UFS	—	$r<0$ & $S2<0$	—	complex
UN/UN/UN	—	$r<0$ & $q>0$	—	real
SFC	—	—	$r>0$ & $S2>0$	complex
SN/SN/SN	—	—	$q>0$ & $r>0$	real

TABLE 2. Zones of various topologies on $p-q-r$ space, where acronyms are: stable-focus-stretching (SFS), unstable-focus-compressing (UFC), unstable-node/saddle/saddle (UNSS), stable-node/saddle/saddle (SNSS), unstable-focus-stretching (UFS), unstable-node/unstable-node/unstable-node (UN/UN/UN), stable-focus-compressing (SFC), stable-node/stable-node/stable-node (SN/SN/SN).

velocity gradient tensor P, Q, R:

$$P=-A_{ii}, Q=\frac{1}{2}\left(P^2-A_{ij}A_{ji}\right), and$$
$$R=\frac{1}{3}\left(-P^3+3PQ-A_{ij}A_{jk}A_{ki}\right). \tag{4.10}$$

Correspondingly, the normalized invariants (p,q,r) of the local velocity gradient tensor (a_{ij}) are defined as:

$$p=-a_{ii}, q=\frac{1}{2}\left(p^2-a_{ij}a_{ji}\right), \ and$$
$$r=\frac{1}{3}\left(-p^3+3pq-a_{ij}a_{jk}a_{ki}\right). \tag{4.11}$$

Determination of the topology of a fluid particle can also be done using the invariants of the normalized velocity gradient tensor (a_{ij}) as well. Chen *et al.* (1989) categories topological patterns (Table 2) that can be observed in an incompressible field into UNSS, SNSS, SFS, UFC. In compressible flows additional four more major topologies can exist: SFS and SNSNSN in contracting fluid particles and UFS and UNUNUN in expanding fluid particles. Figure 2 shows different topologies existing in different p-planes in p-q-r space. Figure 3 present schematics of these topological patterns. The reader is referred to Chong *et al.* (1990) and Suman & Girimaji (2010*b*) for further details on topology.

Since the value of the three invariants of the velocity gradient tensor uniquely determines the topology associated with a local fluid particle, the dynamics of topology can be studied in terms of the dynamics of invariants themselves. Using the evolution equation of the velocity-gradient-tensor (Equation 2.7), the time-evolution of invariants (P,Q,R) of the velocity-gradient-tensor A_{ij} can be found out (Bechlars & Sandberg (2017)):

$$\frac{dP}{dt}=P^2-2Q-S_{ii},$$
$$\frac{dQ}{dt}=QP-\frac{2P}{3}S_{ii}-3R-A_{ij}S^*_{ji},$$

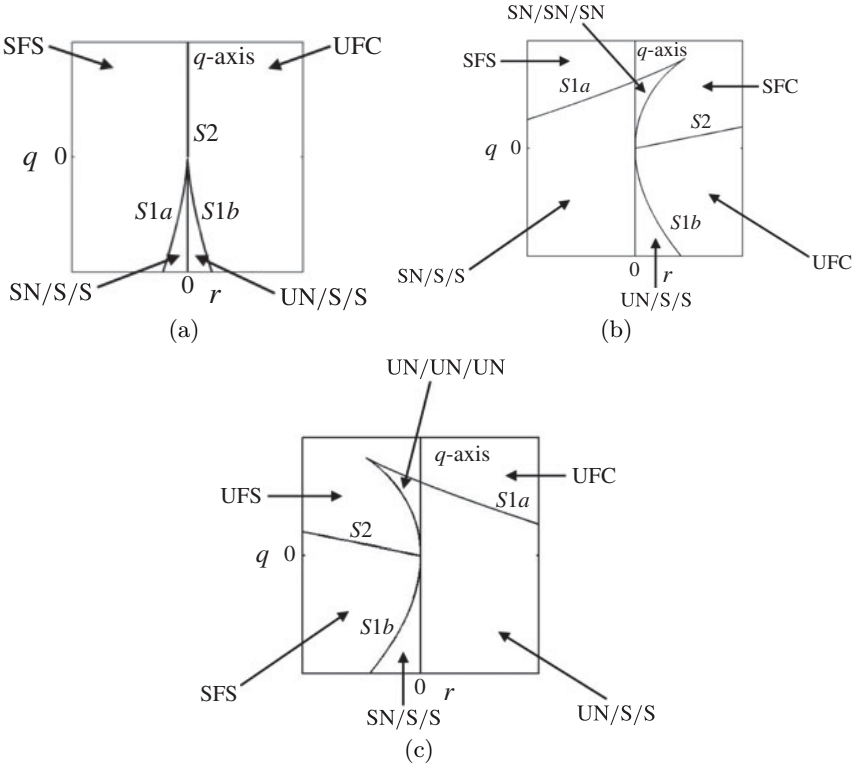

FIGURE 2. Flow topologies represented in different p-planes: a) $p = 0$, b) $p > 0$ and c) $p < 0$. (Figures to be reproduced with permission from Suman & Girimaji (2010*a*).)

$$\frac{dR}{dt} = -\frac{Q}{3}S_{ii} + PR - PA_{ij}S^*_{ji}) - A_{ik}A_{kj}S^*_{ji} \tag{4.12}$$

where, S_{ij} is the source term in the evolution equation of velocity-gradient-tensor (Equation 2.7) and S^*_{ij} is the traceless part of S_{ij} tensor defined as:

$$\begin{aligned} S_{ij} &= -\mathbb{P}_{ij} + \Upsilon_{ij}, \ and \\ S^*_{ij} &= S_{ij} - \frac{S_{kk}}{3}\delta_{ij}. \end{aligned} \tag{4.13}$$

Here $\mathbb{P}_{ij}$ is the pressure hessian tensor and Υ_{ij} represents the contribution of viscosity in the evolution equation of the velocity-gradient tensor (A_{ij}), as shown in Equation 2.7. The relation between non-normalized invariants (P,Q,R) and normalized invariants (p,q,r) is shown in equation 4.14:

$$p = \frac{P}{\sqrt{A_{ij}A_{ij}}}, q = \frac{Q}{A_{ij}A_{ij}}, \ and \ r = \frac{R}{(A_{ij}A_{ij})^{3/2}} \tag{4.14}$$

Subsequently, using equations (4.12 & 4.14), the evolution equation of normalized invariants (p,q,r) can be derived:

$$\begin{aligned} \frac{dp}{dt} = \frac{d}{dt}\left(\frac{P}{\sqrt{A_{ij}A_{ij}}}\right) &= \frac{1}{\sqrt{A_{ij}A_{ij}}}\frac{dP}{dt} - \frac{P}{(A_{ij}A_{ij})^{3/2}}A_{ij}\frac{dA_{ij}}{dt}, \\ \frac{dq}{dt} = \frac{d}{dt}\left(\frac{Q}{A_{ij}A_{ij}}\right) &= \frac{1}{A_{ij}A_{ij}}\frac{dQ}{dt} - \frac{2Q}{(A_{ij}A_{ij})^2}A_{ij}\frac{dA_{ij}}{dt}, \end{aligned}$$

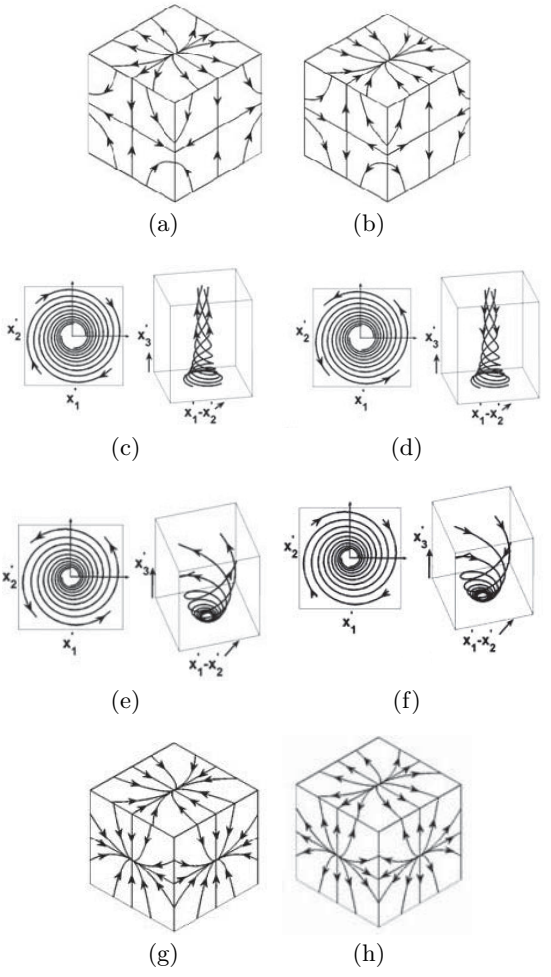

FIGURE 3. Flow patterns corresponding to different flow topologies: a) UNSS, b) SNSS, c) SFS, d) UFC, e) UFS, f) SFC, g) SNSNSN and h)UNUNUN. (Figures to be reproduced with permission from Suman & Girimaji (2010*a*).)

$$\frac{dr}{dt} = \frac{d}{dt}\left(\frac{R}{(A_{ij}A_{ij})^{3/2}}\right) = \frac{1}{(A_{ij}A_{ij})^{3/2}}\frac{dQ}{dt} - \frac{3R}{(A_{ij}A_{ij})^{5/2}}A_{ij}\frac{dA_{ij}}{dt}. \tag{4.15}$$

While following a fluid particle in physical space and tracking its invariants information, we can track the movement of the fluid particle in the p-q-r space. We refer to such a trajectory of the fluid particle in p-q-r space as the Lagrangian trajectory (LT). Mean Lagrangian trajectory (MLT) can be obtained by calculating the mean position of a selected number of particles originating from the same location in p-q-r space (within a specified tolerance) at some reference time (t_{ref}). Note that this procedure involves no approximation.

As mentioned in the Introduction, many researchers have adopted an alternate though approximate procedure of examining trajectories in the p-q-r space. This alternative method does not track the individual fluid particles, but uses the averaged value of the RHS of Equation 4.15 conditioned on a chosen set of p,q,r. In this method, merely a one-time Eulerian dataset of the flow field is used. The statistics thus obtained are essentially the conditional averages of the rate of change of the invariants with the

conditional parameters being the local values of p,q and r. The trajectories thus obtained are basically instantaneous streamlines in p-q-r space. Such trajectories are referred to as the conditional mean trajectories (CMT) (Martín *et al.* 1998).

CMTs are approximate, and their use in past can only be justified as a surrogate tool in the absence of adequate computational resources (Martín *et al.* 1998). In §6.1, with enough resources to calculate MLTs, we compare CMTs against MLTs and evaluate the extent to which CMTs can still be useful as a tool to study topology dynamics in compressible turbulence. Subsequently in §6.2 we employ LTs to investigate mean lifetimes of various topologies, and the influence of initial M_t, Re_λ and dilatation (a_{ii}) on them. To identify the lifetime of topologies, we track a large number of initially identified fluid particles using our DNS datasets and the Lagrangian particle tracker. Particle tracking is performed over a long duration ($\approx 4\tau$) and the residence time of each particle in various topological regions in the p-q-r space is recorded. Subsequent averaging of these residence times (one corresponding to each topology) over a number of fluid particles is thus examined as the mean life of that particular topology. Further details are provided along with results and discussion in §6.2.

5. Lagrangian investigations on the viscous process of velocity gradients

We first analyze the evolution of the exact viscous term in §5.1. After understanding the evolution characteristics of the exact viscous term, we then compare the performance of the LLDM model term in approximating the exact viscous process in §5.2.

5.1. *DNS based examination of viscous process*

In Equation 4.1 we decompose the exact viscous process Υ_{ij} into $\Upsilon_{I_{ij}}$, $\Upsilon_{II_{ij}}$ and $\Upsilon_{III_{ij}}$: these processes represent diffusion of velocity gradient tensor, viscous Hessian of dilatation and interaction of density gradient with velocity gradient components. At this point it is pertinent to examine the relative importance of the three constituent process in a compressible turbulent flow field. For this examination we define three fractions (f_I, f_{II}, f_{III}):

$$f_I = \frac{\sqrt{\Upsilon_{I_{ij}}\Upsilon_{I_{ij}}}}{\sqrt{\Upsilon_{I_{ij}}\Upsilon_{I_{ij}}} + \sqrt{\Upsilon_{II_{ij}}\Upsilon_{II_{ij}}} + \sqrt{\Upsilon_{III_{ij}}\Upsilon_{III_{ij}}}};$$
$$f_{II} = \frac{\sqrt{\Upsilon_{II_{ij}}\Upsilon_{II_{ij}}}}{\sqrt{\Upsilon_{I_{ij}}\Upsilon_{I_{ij}}} + \sqrt{\Upsilon_{II_{ij}}\Upsilon_{II_{ij}}} + \sqrt{\Upsilon_{III_{ij}}\Upsilon_{III_{ij}}}},$$
$$f_{III} = \frac{\sqrt{\Upsilon_{III_{ij}}\Upsilon_{III_{ij}}}}{\sqrt{\Upsilon_{I_{ij}}\Upsilon_{I_{ij}}} + \sqrt{\Upsilon_{II_{ij}}\Upsilon_{II_{ij}}} + \sqrt{\Upsilon_{III_{ij}}\Upsilon_{III_{ij}}}}. \tag{5.1}$$

Clearly, $0 \leqslant f_I \leqslant f_{II} \leqslant f_{III}$. Any of these fraction approaching unity can be used as an evidence of the corresponding process to be the dominant process. Using the flow-field at peak dissipation time from several simulations (B-G, Table 1), we have computed the volume-averaged values of f_I, f_{II} and f_{III}. We find that in all these simulations $f_I \approx 0.9$, $f_{II} \approx 0.09$ and $f_{III} \approx 0.01$. Based on these findings, we conclude that for the range of Mach number and Reynolds number considered in this study, the exact process Υ_{ij} is almost solely represented by $\Upsilon_{I_{ij}}$, itself. Thus in the rest of this study we focus only on $\Upsilon_{I_{ij}}$ and assume it to be almost synonymous with Υ_{ij}. Accordingly, the ratio $\langle r(t, t_{ref})\rangle$

defined earlier in Equation 4.5 is redefined as:

$$r(t, t_{ref}) = \frac{\sqrt{\Upsilon_{I_{ij}}(t)\Upsilon_{I_{ij}}(t)}}{\sqrt{\Upsilon_{I_{ij}}(t_{ref})\Upsilon_{I_{ij}}(t_{ref})}}. \tag{5.2}$$

To understand the influence of initial M_t, in Figure 4 we present Lagrangian mean of $\langle r(t, t_{ref})\rangle$ from simulations E-G. In both case, $t_{ref} = 0.5\tau$. In both simulations this time instant is smaller than the time of peak dissipation event. In each of these simulations, the exact viscous process shows a two-stage evolution. In the first stage of evolution, $\langle r(t, t_{ref})\rangle$ increases and reaches a peak value. In the second stage, it decays in magnitude. This evolution pattern is reminiscent of the evolution of dissipation itself. Indeed the time instant of the peak of dissipation and that of the viscous process match ($t_{peak-dissipation} = 2\tau$). The amplification in the first stage can be attributed to steepening of gradients due to the rapid spread of the spectrum. The decay in the second stage of evolution can be attributed mainly to the decay in kinetic energy. We observe that as initial M_t increases, the peak value of $\langle r(t, t_{ref})\rangle$ increases.

In several previous studies like Suman & Girimaji (2010*b*) and Parashar *et al.* (2017*a*), it has been demonstrated that even when the unconditioned Eulerian or Lagrangian statistics obtained using DNS data of homogeneous turbulence do not show any discernible influence of a global compressiblity parameter like M_t, the same statistics when conditioned upon appropriate local compressibility parameters like normalized dilatation (a_{ii}) and local topology ($\mathcal{T}$) reveal, significant variations and insightful physics. Examining the influence of local local parameters like a_{ii} and $\mathcal{T}$ on turbulence processes is especially useful from the point of view of Lagrangian based statistical closure of turbulence (Lagrangian PDF methods, Pope (2002))., wherein dynamical equations are typically cast in terms of local flow variables directly. Thsus to gain further insight, into the viscous diffusion process ($\Upsilon_{I_{ij}}$), we subject $\langle r(t, t_{ref})\rangle$ to conditioned averaging on discreate values of a_{ii} at t_{ref}. In Figure 5 we present conditional Lagrangian mean of $\langle r(t, t_{ref})\rangle$ from Simulation G, with a_{ii} as the conditioning parameter. In Figure 5a, separate curves are presented for $a_{ii} = -1.0, -0.75, -0.50, -0.25$ and 0, whereas in Figure 5b separate curves are presented for $a_{ii} = 1.0, 0.75, 0.50, 0.25$ and 0. In both figures we observe profound influence of both the magnitude and the sign of a_{ii} on the evolution of $\langle r(t, t_{ref})\rangle$. Even though almost at all dilatation levels, $\langle r(t, t_{ref})|a_{ii}\rangle$ seem to retain the two-stage evolution patterns as shown by the unconditioned statistics $\langle r(t, t_{ref})\rangle$, the extent to which magnification of $\langle r(t, t_{ref})\rangle$ happens (Figure 5) seems to be strongly affected by the value of a_{ii} that a fluid particle has at $t = t_{ref}$. In Figure 5a we observe that as the dilatation level change from being zero (volume preserving fluid particles) to being more negative (contracting fluid particles), the peak value of $\langle r(t, t_{ref})|a_{ii}\rangle$ reduces. On the other hand, in Figure 5b we observe the opposite trend. For fluid particles with high poistive dilatation (expanding fluid particles) the peak value of $\langle r(t, t_{ref})|a_{ii}\rangle$ tends to increase.

In our attempt to understand and explain the behaviour observed in Figure 5a, 5b in Figure 7a and 7b we present the mean value of the amplification of the magnitude of the velocity gradient tensor A_{ij} itself, following the same set of fluid particles as used in Figures 5. We measure this amplification as:

$$\langle r_A(t, t_{ref})\rangle = \left\langle \frac{A_{ij}(t)A_{ij}(t)}{A_{ij}(t_{ref})A_{ij}(t_{ref})} \right\rangle. \tag{5.3}$$

We observe that over almost the entire range of dilatation considered in this work, the trend shown by $\langle r_A(t, t_{ref})|a_{ii}\rangle$ is similar to $\langle r(t, t_{ref})|a_{ii}\rangle$. Like $\langle r(t, t_{ref})|a_{ii}\rangle$, a more positive dilatation tends to move the peak of $\langle r_A(t, t_{ref})|a_{ii}\rangle$ higher and a more negative

dilatation tends to lower the peak of $\langle r_A(t, t_{ref})|a_{ii}\rangle$. One to one correspondence between the trends shown by $\langle r(t, t_{ref})|a_{ii}\rangle$ in Figure 5 and that shown by $\langle r_A(t, t_{ref})|a_{ii}\rangle$ in Figure 7 is not completely unexpected, and it indeed substantiates a gradient diffusion like hypothesis which assumes $\Delta A \propto A$. However, in the light of Figure 7a, 7b our primary curiosity that why the peaks of $\langle r(t, t_{ref})\rangle$ (in Figure 5a, 5b) rise for expanding fluid particles and reduce for contracting fluid particles can now possibly be explained based on the behaviour of A_{ij} itself. In Figure 9a we show $\left\langle \sqrt{A_{ij}(t)A_{ij}(t)}\middle| a_{ii} \right\rangle$ at two time instants, t_{ref} and $t_{ref} + \tau/2$. We observe that the one time statistics of $\left\langle \sqrt{A_{ij}(t)A_{ij}(t)}\middle| a_{ii} \right\rangle$ does not show significant variations with time.

The dependence of $\sqrt{A_{ij}A_{ij}}$ on a_{ii} is monotonic and alomost linear for $a_{ii} > 0$. A faster expanding fluid particle (large positive a_{ii}) is associated with smaller $\sqrt{A_{ij}A_{ij}}$ than a slower expanding fluid particle (small positive a_{ii}). On the other hand contracting particles show a more complex behaviour. Extremely fast contracting particles (very high negative a_{ii}) have a very large $\sqrt{A_{ij}A_{ij}}$. As dilatation decomes less negative $\sqrt{A_{ij}A_{ij}}$ drops first (till $a_{ii} \approx 0.25$) and then again tends to be larger. Thus the dependence of $\sqrt{A_{ij}A_{ij}}$ on a_{ii} is non-monotonic as well as (apparently) non-linear. (Figure 9a) In Figure ?xxxxxxxxxx?a we present averaged rate of change in dilatation (ψ) of tagged fluid particles over one Kolmogorov time:

$$\psi = \left(a_{ii}(\tau_\kappa + t_{ref}) - a_{ii}(t_{ref})\right)/\tau_\kappa, \tag{5.4}$$

where, τ_κ is the Kolmogorov time at t_{ref}. In Figure ?xxxxxxxxxx?b we present the fraction of particles having increased/decreased their a_{ii} over one Kolmogorov time relative to the dilatation the particles had at t_{ref}. We observe that expanding particles are more associated with negative ψ and contracting particles are associated with positive ψ. IN other words, both contracting and expanding fluid particles tend to reduce the magnitude of their dilatation. Since particles with higher inital dilatation tend to acquire lower positive dilatation levels and the associated $\sqrt{A_{ij}A_{ij}}$ of particles with higher positive dilatation is larger than those with lower positive dilatation, it is plausible to expect that the peak of $\langle r(t, t_{ref})\rangle$ will be more at higher positive dilatation than that at lower positive dilatation. Indeed this behaviour is observed in Figure 5a. For contracting particles the dynamics seem to be more complicated because of non-monotonic and highly non-linear distribution of $\langle \sqrt{A_{ij}A_{ij}}|a_{ii}\rangle$ (Figure 9a). At low negative dilatation (say $aii \approx 0.25$), the dominant tendency of particles is to move towards zero dilatation (Figure 9a). The association of higher $\sqrt{A_{ij}A_{ij}}$ at zero dilatation comare to that at low negative dilatation still allows $\langle r_A(t, t_{ref})|a_{ii}\rangle$ to show a substantial magnification at early times (Figure 7a). However, the relatively value of $\sqrt{A_{ij}A_{ij}}$ at low negative dilatation (say -0.25) as compared to that at low positive dilatation say $a_{ii} = +0.25$ (Figure 9a) seem to somewhat restrict the peak value of $\langle r_A(t, t_{ref})|a_{ii}\rangle$ of particles with small negative dilatation when compared to peak value of $\langle r_A(t, t_{ref})|a_{ii}\rangle$ of particles with small positive dilatations (compare the curve of $a_i i = -0.25$ in Figure 7b to the curve of $a_{ii} = -0.25$ in Figure 7a).

For faster contracting particles (say those with initial $a_{ii} \approx -0.75$), Figure 9a shows that (like other contracting particles) they begin their journey towards zero dilatation. However, Figure 9a suggests that as their dilatation reduces, $\sqrt{A_{ij}A_{ij}}$ severely drops (almost exponential drop). This tendency, combined with the fact that initially also they had a high value of $\sqrt{A_{ij}A_{ij}}$, results into dramatic drop in $\langle r_A(t, t_{ref})|a_{ii}\rangle$ as observed in Figure 7a. In summary, in this section we demonstrated that even though the viscous

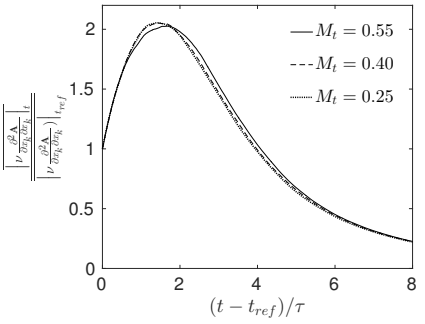

FIGURE 4. Mach number dependence on evolution of exact viscous term ($t_{ref} = 0.5\tau$).

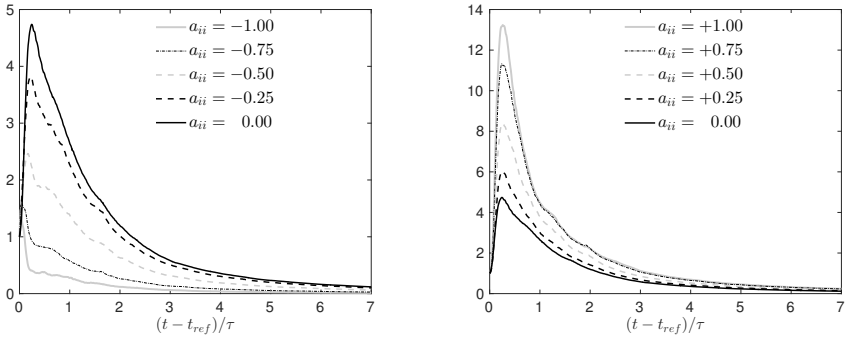

FIGURE 5. Dependence of dilatation rate on evolution of exact viscous term ($t_{ref} = 0.5\tau$).

process ?xxxxxxxxxxxxx? influence of global parameters like M_t, it shows profound influence of local nomralized dilatation rate. All expanding fluid particles when followed tend to undergo magnification of the viscous process. On the other hand contracting particles show reduced magnification tendency. Fast contracting particles seem to show even less magnification thatn slow contracting fluid particles. Further, we showed that this disparate behaviour of the viscous process in contracting and expanding particles is attributable to the vastly different values of $\sqrt{A_{ij}A_{ij}}$ associated with these fluid particles in compressible turbulence and the dominant tendency of these particles to move towards zero dilatation.

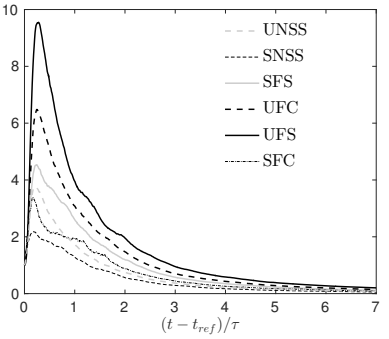

FIGURE 6. Dependence of topology on evolution of exact viscous term ($t_{ref} = 0.5\tau$).

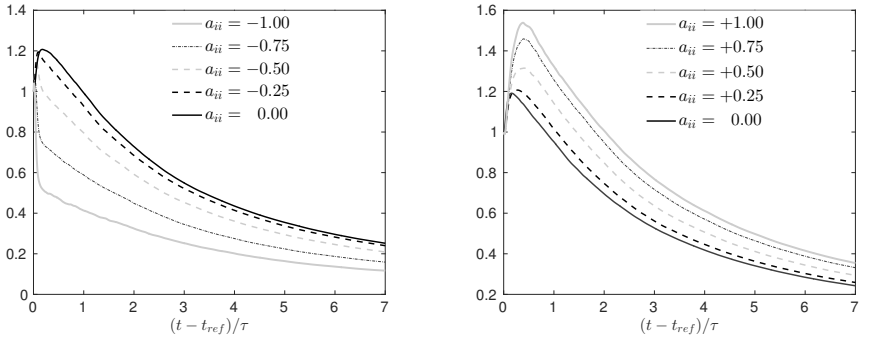

FIGURE 7. Dependence of dilatation rate on evolution of A ($t_{ref} = 0.5\tau$).

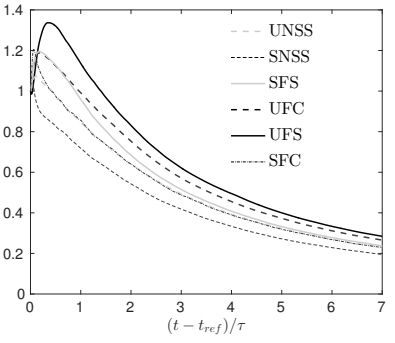

FIGURE 8. Dependence of topology on evolution of A ($t_{ref} = 0.5\tau$).

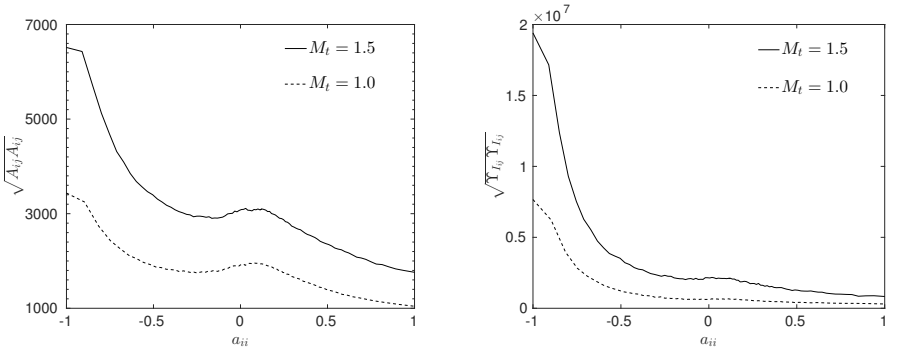

FIGURE 9. Variation in magnitude of a) A_{ij} and b) $\Upsilon_{I_{ij}}$ tensor with dilatation a_{ii} ($t_{ref} = 0.5\tau$).

5.2. *Evaluation of the LLDM model*

Having examined the behavior of the exact process $\Upsilon_{I_{ij}}$ following fluid particles, now we examine the performance of the LLDM model of Jeong & Girimaji (2003), which intends to capture the essential physics of this exact process. For this examination, we use the results of Simulation G (same as what has been used in §5.1). The LLDM modelling approach of Jeong & Girimaji (2003) uses Lagrangian-Eulerianchange in variables to cast $\Upsilon_{I_{ij}}$ as:

$$\nu \frac{\partial^2 A_{ij}}{\partial x_k \partial x_k} = \nu \frac{\partial}{\partial x_k} \left(\frac{\partial X_m}{\partial x_k} \frac{\partial A_{ij}}{\partial X_m} \right), \tag{5.5}$$

where, X_i and x_i are Eulerian and Lagrangian spatial co-ordinates. Further expansion of RHS of Equation 5.5 leads to:

$$\nu \frac{\partial^2 A_{ij}}{\partial x_k \partial x_k} = \underbrace{\nu \frac{\partial X_n}{\partial x_k} \frac{\partial X_m}{\partial x_k} \frac{\partial^2 A_{ij}}{\partial X_m \partial X_n}}_{A} + \underbrace{\nu \frac{\partial A_{ij}}{\partial X_m} \frac{\partial^2 X_m}{\partial x_k \partial x_k}}_{B}. \tag{5.6}$$

$$\tag{5.7}$$

Jeong & Girimaji (2003) neglects term B (first modelling assumption) on the RHS of Equation 5.6 to arrive at the following equation:

$$\nu \frac{\partial^2 A_{ij}}{\partial x_k \partial x_k} \approx \nu \frac{\partial X_n}{\partial x_k} \frac{\partial X_m}{\partial x_k} \frac{\partial^2 A_{ij}}{\partial X_m \partial X_n}. \tag{5.8}$$

$$\tag{5.9}$$

Using the definition of the deformation gradient tensor D_{ij} (Equation 4.3) and the right Cauchy-Green tensor C_{ij} (Equation 4.4), the RHS of Equation 5.8 can be expressed in terms of C_{ij}:

$$\frac{\partial X_n}{\partial x_k} \frac{\partial X_m}{\partial x_k} = D_{kn}^{-1} D_{km}^{-1} \tag{5.10}$$

$$\frac{\partial X_n}{\partial x_k} \frac{\partial X_m}{\partial x_k} = (D_{km} D_{kn})^{-1} \tag{5.11}$$

$$\nu \frac{\partial^2 A_{ij}}{\partial x_k \partial x_k} \approx \nu C_{mn}^{-1} \frac{\partial^2 A_{ij}}{\partial X_m \partial X_n} \tag{5.12}$$

$$\tag{5.13}$$

Further, Jeong & Girimaji (2003) make the second modelling assumption wherein C_{mn}^{-1} is approximated as an isotropic tensor:

$$\nu \frac{\partial^2 A_{ij}}{\partial x_k \partial x_k} \approx \nu \frac{C_{kk}^{-1}}{3} \delta_{mn} \frac{\partial^2 A_{ij}}{\partial X_m \partial X_n} \tag{5.14}$$

$$\nu \frac{\partial^2 A_{ij}}{\partial x_k \partial x_k} \approx \nu \frac{C_{kk}^{-1}}{3} \frac{\partial^2 A_{ij}}{\partial X_m \partial X_m} \tag{5.15}$$

$$\tag{5.16}$$

Finally, the third approximation is made ($\frac{\partial^2 A_{ij}}{\partial X_m \partial X_m} = \frac{A_{ij}}{\delta X^2}$)

$$\nu \frac{\partial^2 A_{ij}}{\partial x_k \partial x_k} \approx \nu \frac{C_{kk}^{-1}}{3} \frac{A_{ij}}{(\delta X)^2} \tag{5.17}$$

$$\nu \frac{\partial A_{ij}}{\partial x_k \partial x_k} \approx \frac{C_{kk}^{-1}}{3\tau_\nu} A_{ij} \tag{5.18}$$

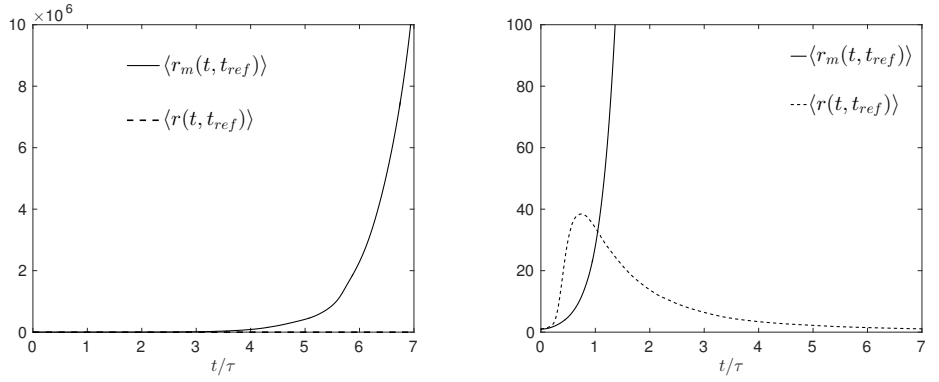

FIGURE 10. Comparison of LLDM model term and the exact viscous term: a) unscaled axis, b) axis scaled to visualize the difference in growth rates of the two processes.

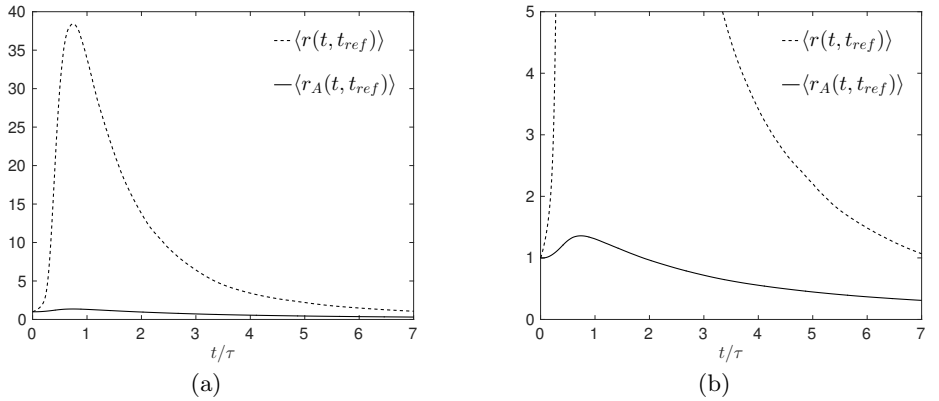

FIGURE 11. Evolution of magnitude of velocity gradient tensor $|A|$.

The evolution equation of the deformation gradient tensor (D_{ij}) is:

$$\frac{dD_{ij}}{dt} = D_{ik}A_{kj}. \tag{5.19}$$

τ_ν is the molecular viscous relaxation time scale, defined as:

$$\tau_\nu = \delta X^2/\nu \approx \lambda_\tau^2/\nu, \tag{5.20}$$

where, λ_τ is Taylor microscale.

In Figure 10, we compare the LLDM model with the exact viscous term. We observe that unlike the evolution of the exact process, the LLDM model term shows monotonic growth with time. At the early stages of evolution, the monotonic growth is at least qualitatively the same as the exact process. However, at later stages (after the dissipation peak event) this continued monotonic growth in is gross disagreement with the decaying behavior of the exact process after reaching a peak value. In Figure 11 we present the evolution of $|A|$ with time. We observe that $|A|$ does show a two-stage behavior and starts decaying after the peak dissipation event. Comparing Figure 10 and Figure 11, it is clear that the coefficient C_{kk}^{-1} of the LLDM model grossly overestimates the influence of the C^{-1} tensor.

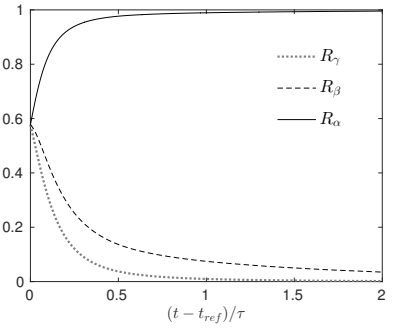

FIGURE 12. Evolution of locally normalized eigenvalues of C^{-1}

To better understand the reason for the failure of the LLDM model, we revisit the modelling assumptions. One of the assumptions used in the model is that the tensor C^{-1} is isotropic. To scrutinize whether this assumption is contributing to the model failure, we examine the eigenvalues of the C^{-1} tensor. The C^{-1} tensor is always symmetric (since $C = DD^T$ is symmetric), hence the eigenvalues of C^{-1} are always real. To examine the validity of the isotropic assumption, we plot the mean evolution of the three eigenvalues ($\alpha > \beta > \gamma$). In Figure 12 we present the Lagrangian statistics of R_α, R_β and R_γ as a function of time. We observe that the eigenvalues begin to depart from each other. R_α increases appreciably during the evolution phase, while R_β and R_γ decreases to negligible values. This indicates that the C^{-1} tensor is strongly biased towards $\alpha-$eigenvector. Thus, it is clear that the assumption of the isotropy of the tensor is incorrect.

As shown in §4, (Equation 5.17 and 5.18) viscous term in LLDM model can also be recovered by assuming the 4^{th} order tensor $\frac{\partial^2 A_{ij}}{\partial X_m \partial X_n}$ to be isotropic. However, it is not possible to find the eigen-values of this tensor directly. By lagrangian change of variables, $\frac{\partial^2 A_{ij}}{\partial X_m \partial X_n}$ can be approximated as:

$$\frac{\partial^2 A_{ij}}{\partial X_m \partial X_n} \approx \frac{x_m}{X_m}\frac{x_n}{X_n}\frac{\partial^2 A_{ij}}{\partial x_m \partial x_n} \tag{5.21}$$

Since a product of an anisotropic tensor with an isotropic tensor is always anisotropic, we rather evaluate the eigenvalues of $\frac{\partial^2 A_{ij}}{\partial x_m \partial x_n}$ tensor. Since, this tensor is of order 4, we dissociate the tensor into 9 second-order tensors and analyze their eigenvalues. Since, $\frac{\partial^2 A_{ij}}{\partial x_m \partial x_n}$ is not symmetric, it is not guaranteed to have real eigenvalues. Indeed, the eigenvalues of the tensor are not purely real with mean ratio of the imaginary part to the real part for α, β and γ eigenvalues to be 0.13, 0.77 and 0.17 respectively . However, inorder to measure the extent of anisotropy, we plot the ratio of real part of the eigenvalues in terms of R_α, R_β and R_γ in Figure 13. Clearly the $\frac{\partial^2 A_{ij}}{\partial x_m \partial x_n}$ tensor is anisotropic with ratio of the eigenvalues as: $\alpha : \beta : \gamma :: 1.9 : 1.0 : 1.1$. Hence, it can be concluded that the $\frac{\partial^2 A_{ij}}{\partial X_m \partial X_n}$ tensor is also anisotropic.

In summary, our investigations reveal that the performance of the LLDM model is unrealistic in the later stage of evolution of decaying turbulence. In the first stage of evolution, even though qualitatively LLDM captures the right behavior, it tends to overestimate the value. Our investigations reveal that the isotropy assumption of the C^{-1} and $\frac{\partial^2 A_{ij}}{\partial X_m \partial X_n}$ tensor is one of the major cause of the unrealistic behavior of the LLDM model term as compared to the exact viscous term.

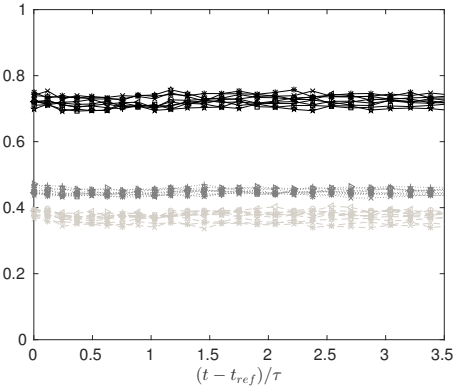

FIGURE 13. Evolution of locally normalized real part of eigenvalues of $\frac{\partial^2 A_{ij}}{\partial x_m \partial x_n}$. Three different colors of the line plot viz. black, light gray, dark gray represents R_α, R_β and R_γ respectively. Different markers represents eigenvalues corresponding to different 2^{nd} order tensors (components) of the original 4^{th} order tensor. R_{ij} represents ratio of normalized eigenvalue for $\frac{\partial^2 A_{ij}}{\partial X_m \partial X_n}$. Different marker identifiers are $\longrightarrow$ +: R_{11}, o: R_{12}, $*$: R_{13}, <: R_{21}, >: R_{22}, x: R_{23}, $\square$: R_{31}, $\bigcirc$: R_{32}, $\pentagon$: R_{33}

6. Comparisons of Eulerian and Lagrangian investigations of flow field topology

In §6.1 we present a comparative study between the CMT and MLT and highlight some important differences between the two. Further in the §6.2 we study the life of topology using LTs and examine the influence of compressibility on it.

6.1. *CMT vs. MLT*

CMT has been extensively used as a method to predict particle trajectories in p-q-r space. CMTs are basically instantaneous streamlines of particles in p-q-r space. Several researchers have drawn conclusions based on the time-integrated behavior of CMT as a complete substitute of MLT. However, using CMT for predicting long-term behaviour−such as finding the life of topology may not be as accurate as MLT. We present a discussion here highlighting the shortcomings of CMT over MLT. As most of the CMT based studies have been performed for incompressible flows (Ooi *et al.* (1999); Meneveau (2011); Lozano-Durán *et al.* (2015)), we use nearly incompressible simulation (case A 1), to demonstrate the difference between CMT and MLT. We further condition the data-set at very small dilatation value ($|a_{ii}| < 0.01$) to assert very weak compressibility effects.

To highlight the difference, we show CMT and MLT emerging from a small region in q-r plane ($p = 0 \pm 0.01$) in Figure 14(a-d) (for all four topologies that exist in this plane). It is evident from Figure 14 that the instantaneous CMT does not coincide with the MLT of fluid particles in q-r plane. There is no directional preference of fluid particles to rotate in spiral order and converge to the origin of q-r plane, as inferred by CMT (Figure 14(a-d)). In-fact the mean trajectory (MLT) converging directly to origin with no tendency to rotate around the origin, explains no directional preference and a clear tendency to randomly move in the q-r space. This argument is further supported by Figure 15(a), where the root-mean-squared value of q and r is plotted with time.

Using the CMT approach, it can be shown that in around 3 eddy-turnover time, a fluid particle completes one complete rotation around the origin (Ooi *et al.* (1999)). However, it can be clearly seen in Figure 15(a), that in just 1 eddy-turnover time, the rms approaches

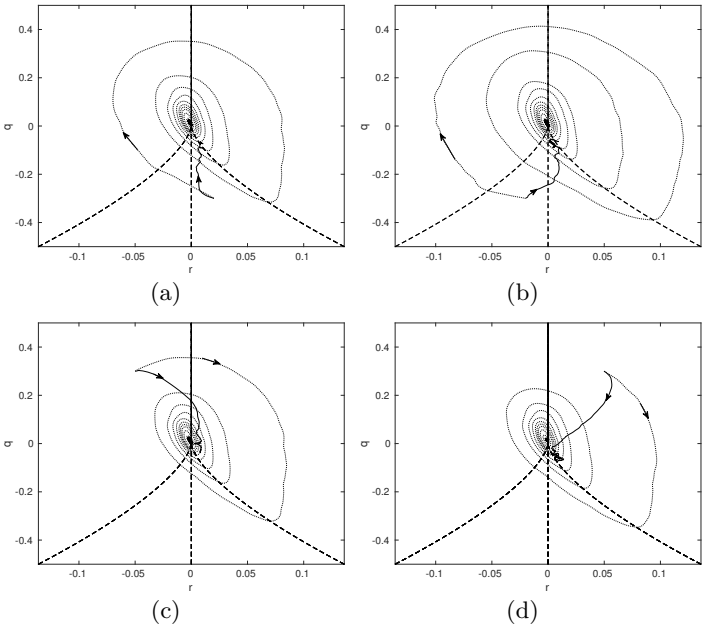

FIGURE 14. Comparison of instantaneous CMTs (dotted line) and actual mean Lagrangian trajectory MLT (solid line) of fluid particles with bin dimensions $r \in \overline{r} \pm 0.01$ and $q \in \overline{q} \pm 0.025$ for (a)UNSS, (b)SNSS, (c)SFS and (d)UFC topology. Dashed lines represent surfaces: S1a, S1b and S2.

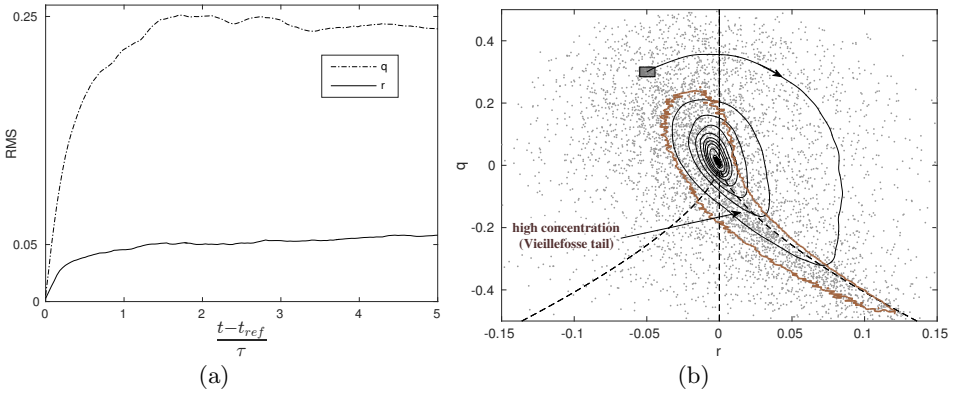

FIGURE 15. (a) Evolution of root mean squared value of invariants q and r starting from a bounded region r (-0.05 ± 0.01) and q (0.3 ± 0.025) (b) Instantaneous CMT (solid line) and final spread of Lagrangian particles after 1 eddy-turnover time starting from the bounded region. Sample size of conditioned particles in the bounded region ≈ 5000.

its maximum value ($q_{rms} \approx 0.24$ and $r_{rms} \approx 0.05$), indicating maximum spread of the fluid particles in q-r plane. In-fact these RMS values are identical to the RMS of q and r location of global unconditioned sample. To further understand this difference, we plot the location of various fluid particles starting from a small region in q-r plane after 1 eddy-turnover time (Figure 15(b)). It can be observed that the population spread after 1 eddy-turnover time, is in-fact similar to the global spread of particles in q-r plane with major concentration along the Vieillefosse tail.

Table 3 shows the percentage topology composition after three eddy-turnover times

	100% UNSS				100% SNSS				100% SFS				100% UFC			
	UNSS	SNSS	SFS	UFC	UNSS	SNSS	SFS	UFC	UNSS	SNSS	SFS	UFC	UNSS	SNSS	SFS	UFC
t_{ref}	100	0	0	0	0	100	0	0	0	0	100	0	0	0	0	100
$t_{ref} + 3\tau$	27	8	38	26	27	8	39	26	23	7	41	28	26	8	39	27

TABLE 3. Percentage topology composition for particles after 3 eddy-turnover time starting with 100% UNSS, SNSS, SFS and UFC sample respectively.

	UNSS	SNSS	SFS	UFC
% anticlockwise	32	51	33	33
% clockwise	68	49	67	67

TABLE 4. Clockwise and anti-clockwise movement of particles in q-r plane. [Note: This table shows percentage transfer of particles. The topology composition remains invariant with time i.e. Total particles moving in and out of a particular topology is same.]

of particles initially belonging to a distinct topology. It is evident that after three eddy-turnover times the particles gets distributed throughout the q-r plane with the final composition identical to global unconditioned sample. In fact, the composition after three eddy-turnover times is approximately equal to the global topology composition for isotropic incompressible flow as reported by Suman & Girimaji (2009). This observation challenges the CMT approach that approximates particle motion in the q-r plane using instantaneous Eulerian flow field. Table 4 shows anticlockwise and clockwise movement of particles starting from a particular topology using LT approach. It can be seen that a significant fraction of particles moves anti-clockwise (1/2 for SNSS topology and 1/3 for UNSS, SFS and UFC topology). Therefore it can be concluded that the CMT approach inaccurately predicts cyclic rotation of particles around the origin.

Hence, from the above analysis, we conclude that CMT does not represent actual motion of fluid particles in q-r plane for incompressible flow. In general, the fluid particles move around randomly in q-r plane, such that at every time instant the overall distribution of particles is identical, with major concentration along the Vieillefosse tail.

Although, the above analysis is performed for incompressible flow, we expect even for compressible flow, the motion of fluid particles to be such that their topology composition approach global topology composition with time. To prove this hypothesis, we show time-evolution of percentage composition of particles originating from a discrete p-plane ($p = +0.5 \pm 0.05$) for compressible simulation E (Table 1) in Figure 16. It can be seen in Figure 16 that despite a significant variation in initial composition of topology as compared to global composition, the particles moves around randomly in p-q-r space such that their percentage composition tends toward the global composition.

6.2. *Life of topology*

In this section, we quantify the life-time of existence of particles in different topologies. Starting with 10,00,000 particles, we tag the particles based on their topology at t_{ref} and track them until they lose their initial topology. The life-time of each particle (l_κ) in a particular topology is measured as a fraction of Kolmogorov time, τ_κ (measured at t_{ref}), calculated by recording the time from t_{ref} to the instant the particle loses it's initial topology. Further, we calculate the life-time of topology (L_κ) as the mean life-time of all

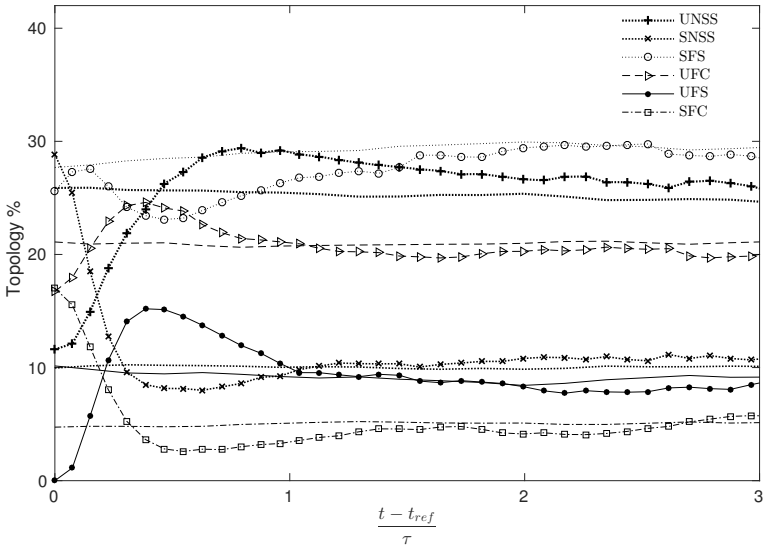

FIGURE 16. Evolution of topology-composition for particles initially conditioned at $p = +0.5 \pm 0.05$ for 6 major topologies viz. UNSS, SNSS, SFS, UFC, UFS, SFS (Simulation E). Initial composition at $t_{ref} = 4\tau$: UNSS = 11.6%, SNSS = 28.9%, SFS = 25.6%, UFC = 16.7%, UFS = 0%, SFC = 17.0%, SNSNSN = 0.2%, UNUNUN = 0%. Lines without markers represents topology composition of global unconditioned sample.

	UNSS	SNSS	SFS	UFC
Sample %	25.2	5.4	43.5	25.9
Life of topology (κ_τ)	1.80	0.53	3.32	2.08
Life %	23.32	6.86	42.95	26.91

TABLE 5. Life of topology L_κ for nearly incompressible flow (case A). The sample is further conditioned on dilatation ($|a_{ii}| < 0.01$) to ensure strong incompressibility. Sample size $\approx$ 1,25,000 particles (conditioned).

the particles in a particular topology (in terms of τ_κ):

$$L_\kappa = \sum_{i=1}^{N} \frac{l_{\kappa_i}}{N} \tag{6.1}$$

6.2.1. *Incompressible flow*

We first show life of topology for nearly incompressible simulation (case A) in Table 5. To assert very mild compressibility, we further condition our sample on dilatation ($|a_{ii}| = |p| < 0.01$). It can be observed that life of topology is proportional to the percentage composition of topology. SFS topology is the most stable with average lifetime of $3.3\kappa_\tau$, next is the UFC topology with average lifetime of $2\kappa_\tau$, next most stable is UNSS with a lifetime of $1.8\kappa_\tau$. SNSS topology is found to be least stable with average lifespan of $0.5\kappa_\tau$. Hence, for incompressible flow, the order of stability of topology is as follows:

$$SFS \longrightarrow UFC \longrightarrow UNSS \longrightarrow SNSS.$$

Table 6 shows the average velocity ($|U_{pqr}| = |\frac{\partial p}{\partial t}\hat{p} + \frac{\partial q}{\partial t}\hat{q} + \frac{\partial r}{\partial t}\hat{r}|$) of particles in different topologies in p-q-r space. It is interesting to observe that although the average velocity

	UNSS	SNSS	SFS	UFC
average velocity $\lvert U_{qr}\rvert$ (units: s^{-1})	0.23	0.28	0.23	0.26

TABLE 6. Average velocity of particles in p-q-r space ($U_{pqr} = \frac{\partial p}{\partial t}\hat{p} + \frac{\partial q}{\partial t}\hat{q} + \frac{\partial r}{\partial t}\hat{r}$) for simulation case A.

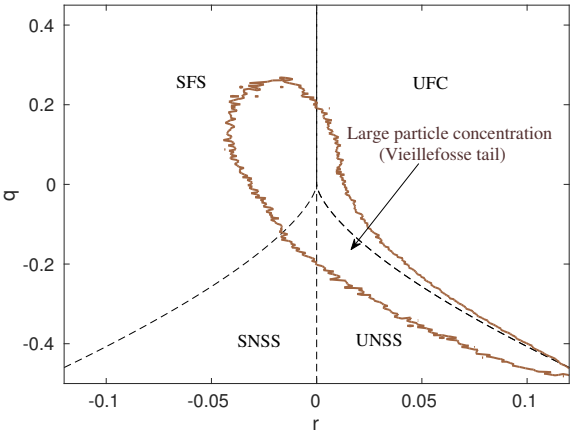

FIGURE 17. Region of high concentration of particles in q-r space.

for different topologies is comparable in magnitude, there is a significant difference in their lifetimes (L_κ). It can also be seen in Table 5, that the proportion of life of different topologies is identical to their percentage composition. To explain the variation in L_κ for different topologies, we focus on the distribution of the population in various zones of topology rather than just percentage composition. Figure 17 shows region of high concentration of particles in q-r plane. This region of high particle concentration is also termed "Vieillofosse tail". It can be seen in Figure 17 that, while SFS and UFC region have an equal area in the q-r plane, their population distribution is not alike. In UFC, the population has a spread closer to the surfaces of unlike topologies, than for SFS topology. Closer proximity to the nearby surfaces of unlike topologies explains the likelihood of UFC to be more prone to change than SFS topology, having known that their average speeds in p-q-r space are comparable in magnitude (Table 6). Similarly, UNSS and SNSS have equal area. Still, UNSS is found to be more stable than SNSS topology. This is because for SNSS topology the bulk of the population is found closer to the origin where nearby surfaces separating different topologies are closer leading to higher probability of particles crossing the zone of SNSS topology into other topologies. However, in UNSS topology, the population although highly concentrated near the origin, has significant population spread away from the origin, where nearby surfaces for interconversion are not very close. Hence, despite having comparable average velocities, different topologies have different lifetimes (L_κ).

6.2.2. *Compressible flow*

We show average life-time of topology for compressible simulations (case E-I) in Table 7. It can be seen that the life-time of topology is again a strong function of particle concentration. In-fact the percentage life of different topologies is almost identical to the composition of their populations (Table 7). However, the order of stability seems to be

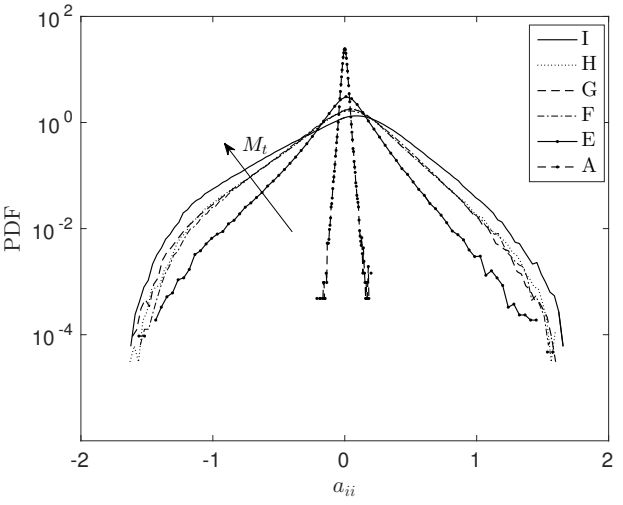

FIGURE 18. PDF of noramilized dilatation a_{ii} for different simulations (Table 1).

influenced by M_t (Table 7). For weakly compressible flow (simulation A), the order of stability based on lifetime for four major topologies is $SFS \longrightarrow UNSS \longrightarrow UFC \longrightarrow SNSS$. However, global turbulent Mach number of the flow seems to affect the order of stability.

To explain this variation in the order of stability with M_t, we now focus on the localized origin of compressibility. As shown by Suman & Girimaji (2010*a*), the extent of compressibility can be determined solely by the strength of dilatation ($-\sqrt{3} < a_{ii} < \sqrt{3}$). Compressibility is a localized phenomenon, i.e., regions of weak and strong compressibility are present in the flow field. However, statistically, by looking at the probability-density-function (PDF) of dilatation one can determine the extent of compressibility. A larger spread of the dilatation PDF, represent a high strength of compressibility. For incompressible flow ($a_{ii} = -p \approx 0$), only 4 flow topologies exist viz. UNSS, SNSS, SFS and UFC topology. But compressibility gives rise to new flow-topologies (Figure 2), existing in p-q-r space in planes of non-zero dilatation ($|p| > 0$). The population of these topologies depends upon the spread of dilatation. Weak compressibility, accompanied by low dilatation spread leads to a low population of topologies existing in non-zero p-planes and vice-versa for highly compressible flow. In Figure 18, we show the PDF of dilatation for different simulations. It can be seen that the dilatation spread increases with turbulent Mach number. However, there seems to be little to no dependence on Reynolds number as evident from simulations F-H (Figure 18).

From the above discussion, it can be concluded that there is no general order of stability of topology for compressible flows. However, for major 4 topologies (UNSS, SNSS, SFS and UFC), there is a particular order of stability:

$$SFS \longrightarrow UNSS \longrightarrow UFC \longrightarrow SNSS.$$

Further, at very high Mach numbers the order stability based on life-time of existence is found to be as follows:

$$SFS \longrightarrow UNSS \longrightarrow UFC \longrightarrow UFS \longrightarrow SNSS \longrightarrow SFC \longrightarrow UNUNUN \longrightarrow SNSNSN.$$

In order to explain the variation of lifetime of topology with M_t, we report the

Simulation		UNSS	SNSS	SFS	UFC	UFS	SFC	SNSNSN	UNUNUN
case A	Sample %	25.2	5.4	43.5	25.9	0	0	0	0
M=0.075	Life of topology	1.80	0.53	3.32	2.08	0	0	0	0
R = 70	Life %	23.32	6.86	42.95	26.91	0	0	0	0
case E	Sample %	24.68	8.35	33.78	21.67	5.17	4.53	0.09	0.09
M=0.6	Life of topology (κ_τ)	1.31	0.44	1.80	1.15	0.28	0.24	0.05	0.05
Re=350	Life %	24.62	8.27	33.83	21.62	5.26	4.51	0.01	0.01
case F	Sample %	27.81	10.26	28.42	20.88	8.44	3.89	0.14	0.15
M=1	Life of topology (κ_τ)	1.04	0.31	1.13	0.85	0.35	0.24	0.06	0.11
Re=150	Life %	25.43	7.58	27.63	20.78	8.56	5.87	1.47	2.69
case G	Sample %	26.61	9.82	26.26	21.50	8.39	4.14	0.14	0.14
M=1	Life of topology (κ_τ)	1.01	0.31	1.18	0.86	0.35	0.25	0.06	0.10
Re=100	Life %	24.51	7.52	28.64	20.87	8.50	6.07	1.46	2.43
case H	Sample %	26.52	9.45	29.96	21.52	8.08	4.23	0.13	0.10
M=1	Life of topology (κ_τ)	1.00	0.29	1.20	0.86	0.33	0.24	0.06	0.08
Re=70	Life %	24.63	7.14	29.56	21.18	8.13	5.91	1.48	1.97
case I	Sample %	26.07	10.10	27.44	21.16	10.49	4.32	0.23	0.21
M=1.5	Life of topology (κ_τ)	0.87	0.26	0.94	0.74	0.35	0.23	0.07	0.09
Re=70	Life %	24.51	7.32	26.48	20.85	9.86	6.48	1.97	2.54

TABLE 7. Life of topology for compressible flows (case A, E-I). Sample size = 10,00,000 particles.

Simulation	UNSS	SNSS	SFS	UFC	UFS	SFC	SNSNSN	UNUNUN
A	0.23	0.28	0.23	0.26	-	-	-	-
E	0.58	0.88	0.60	0.66	0.62	0.96	2.6	1.80
F	0.86	1.39	0.95	1.00	0.82	1.55	2.15	1.33
G	0.84	1.35	0.92	0.99	0.80	1.49	2.35	1.21
H	0.88	1.37	0.97	1.03	0.87	1.46	1.87	1.37
I	1.01	1.57	1.13	1.18	0.90	1.76	1.94	1.27

TABLE 8. Average velocity of particles in p-q-r space ($|U_{pqr}| = |\frac{\partial p}{\partial t}\hat{p} + \frac{\partial q}{\partial t}\hat{q} + \frac{\partial r}{\partial t}\hat{r}|$) for simulations A and E-I.

magnitude of mean velocities ($U_{pqr} = \frac{\partial p}{\partial t}\hat{p} + \frac{\partial q}{\partial t}\hat{q} + \frac{\partial r}{\partial t}\hat{r}$) of particles in p-q-r space in Table 8. It can be seen that $|U_{pqr}|$ increases with M_t for all major topologies, while for extreme topologies−UNUNUN and SNSNSN, the variation in $|U_{pqr}|$, although most likely opposite, seems less significant as compared to variation in rest of the 6 topologies.

For first 4 topologies (UNSS, SNSS, SFS, UFC), the decrease in life with increasing M_t can be attributed to the increase in $|U_{pqr}|$ with increasing M_t. The rest of the topologies come into existence only at high M_t, hence first their lifetime increases with M_t, but further, with an increase in M_t their lifetime tend to remain constant, despite variation in U_{pqr}.

Further, as can be inferred from simulations F-H in Table 7, the Reynolds number show negligible influence on the lifetime/stability of topology.

6.2.3. *Influence of initial dilatation*

In Figure 19, we present the variation in L_κ for various topologies with initial dilatation (a_{ii}). To explain the variation in L_κ with dilatation we show joint-PDF (JPDF) of particle population in different planes of discrete dilatation in Figure 20. For UNSS topology, peak life-times (L_κ) are observed at 0 dilatation (Figure 19(a)). Particles with UNSS topology having initial positive dilatation have higher life as compared to those with initial negative dilatation. This happens because for UNSS topology, the zone of existence in p-q-r space shrinks along with decrease in population as dilatation decreases from high positive dilatation to negative dilatation as shown in figure 20 (b-f). On the contrary, the region of existence of SNSS topology widens while moving from high positive to high negative population (20 (b-f)). This leads to lower population of SNSS topology at high positive dilatations (Figure 19(b)).

Life-times (L_κ) for SFS and UFC topology are shown in Figure 19(c) and 19(d) respectively. It can be seen that both SFS and UFC topologies exhibit monotonic rise, peaking in value for small positive dilatation, followed by monotonic fall while moving from negative dilatation to positive dilatation. The variation is approximately symmetric, slightly skewed towards positive values of dilatation. Variation ofL_κ with initial dilatation for UFS and SFC topology are shown in Figure 19(e) and 19(f) respectively. UFS and SFC topologies have smaller L_κ and shows small variation with dilatation in their respective regions of existence ($a_{ii} > 0$ for UFS and $a_{ii} < 0$ for SFC).

Hence, effect of initial dilatation is found to be maximum in UNSS and SFS topologies, followed by UFC topology, while other topologies, with low global life-times seem to exhibit mild variation in their life-times with varying initial dilatation.

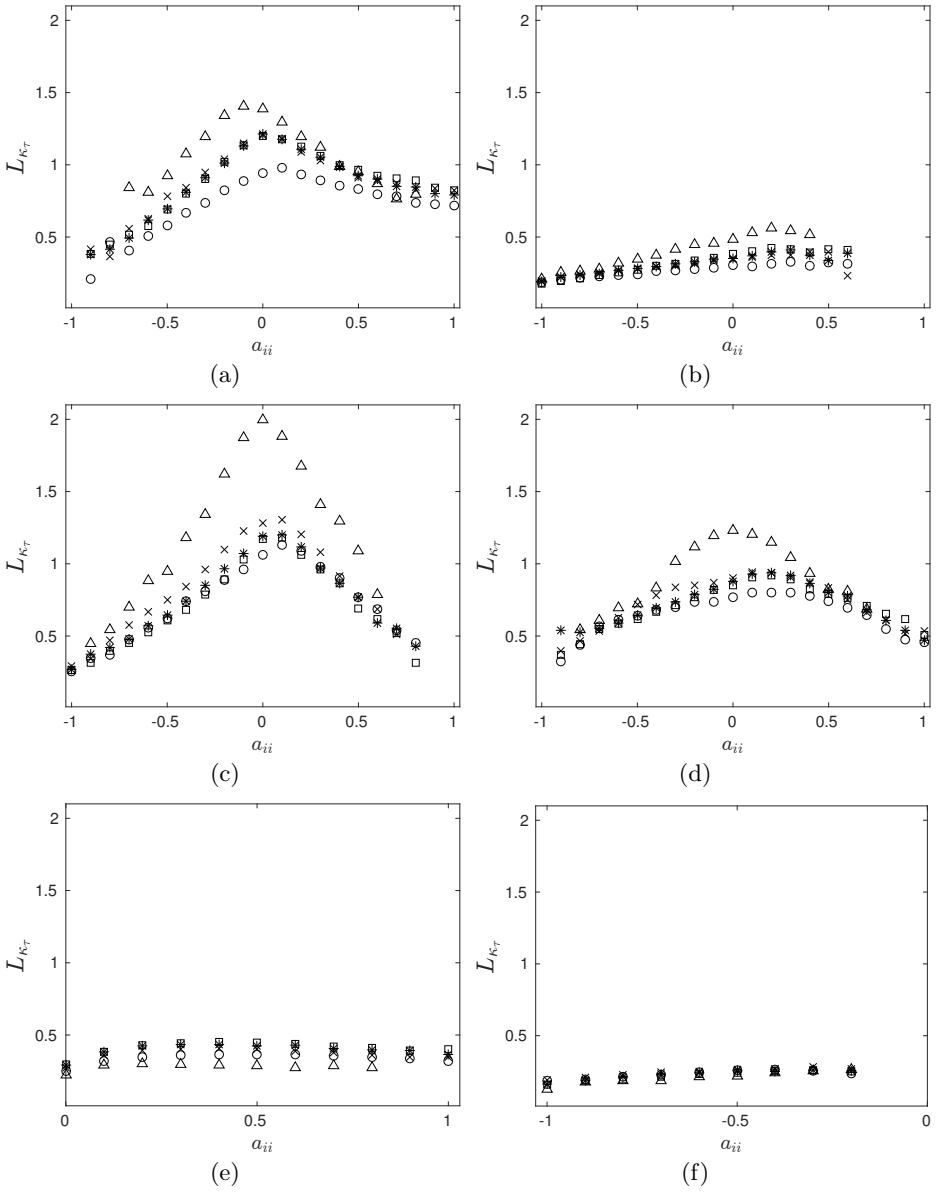

FIGURE 19. Variation of life of topology L_{κ_τ} with initial dilatation a_{ii} (bin size: $\overline{a_{ii}} \pm 0.05$) for 6 major topologies: (a)UNSS, (b)SNSS, (c)SFS, (d)UFC, (e)UFS and (f)SFC. Symbol $\triangle$, $\square$, $*$, $\times$, and O represents life-time of topology for simulations E, F, G, H and I respectively.

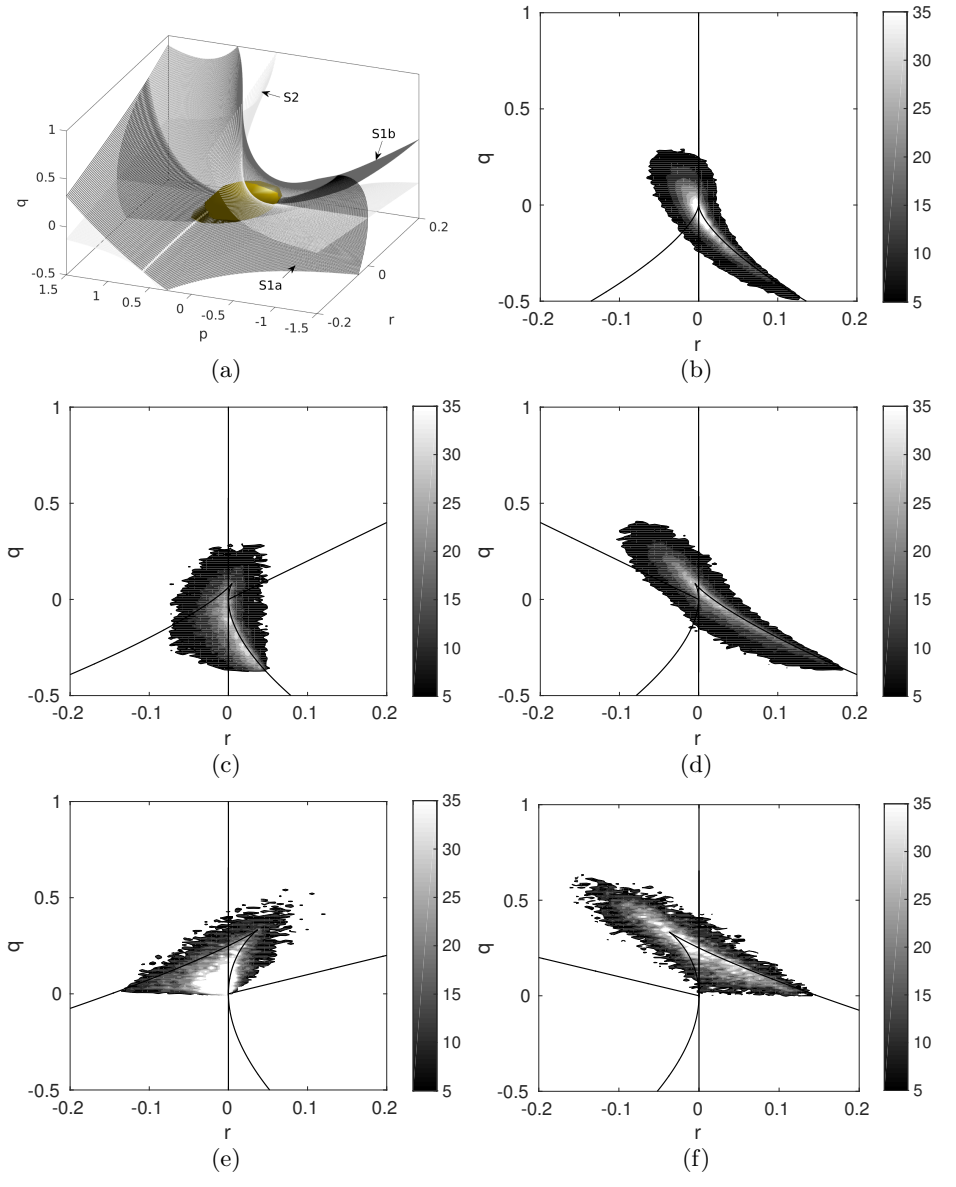

FIGURE 20. Population spread of particles in p-q-r space shown as (a) surface plot of region of high density ($> 50\%$ of maximum density) and Joint-PDF of population of particles at discrete planes of dilatation: (b)$a_{ii} = 0$, (c)$a_{ii} = -0.5$, (d)$a_{ii} = +0.5$, (e)$a_{ii} = -1$, (f)$a_{ii} = +1$

7. Conclusions

We investigate the performance of the LLDM model of Jeong & Girimaji (2003) by comparing the evolution of the LLDM model term with the exact viscous term. Further, we compare the mean Lagrangian trajectory of fluid particles (MLT) with CMT and investigate the lifetime of different topologies using Lagrangian trajectories (LTs). Well-resolved direct numerical simulations (up to 1024^3) of compressible decaying isotropic turbulence with Reynolds number up-to 350 and Mach number up-to 1.5 are employed to perform our studies. Along with this, a spline-interpolation based Lagrangian particle tracker is used to track an identified set of fluid particles (at t_{ref}) and extract their Lagrangian statistics.

We found that the time evolution of the exact viscous term $\left|\frac{\partial^2 A_{ij}}{\partial x_k \partial x_k}\right|$ shows a two-stage behavior. Its evolution is independent of turbulent Mach number. However, it's evolution is intensified at an elevated magnitude of dilatation. Further, we find that the exact viscous process occurs at an amplified rate for rotation dominated topologies as compared to strain-dominated topologies.

While comparing LLDM model term with the exact viscous term, we found that LLDM model grossly overestimates the exact viscous process. LLDM model term undergoes an exaggerated monotonic rise with time, failing to replicate the 2-stage evolution behavior of the exact viscous term. We find that this anomaly in behavior can be attributed to the LLDM modeling assumption of the isotropy of the inverse right Cauchy Green tensor C^{-1} and the $\frac{\partial^2 A_{ij}}{\partial X_m \partial X_n}$ tensor.

The actual motion of fluid particles in p-q-r space seems to show no particular tendency to move in clockwise spiral orbit around the origin, as indicated by instantaneous CMTs. In fact, there seems to be significant movement in the anticlockwise direction as well. A group of chosen fluid particles is found to move randomly such that in very short times ($\approx$ 1 eddy-turnover time) the particles distribution mimics the global distribution, which remains almost constant for fully developed turbulent flow. Computations for mean life-time of topology reveals the following order of stability:

(i) Incompressible:

$$SFS \longrightarrow UFC \longrightarrow UNSS \longrightarrow SNSS$$

(ii) Mildly Compressible:

$$SFS \longrightarrow UNSS \longrightarrow UFC \longrightarrow SNSS \longrightarrow UFS \longrightarrow SFC \longrightarrow UNUNUN \longrightarrow SNSNSN.$$

(iii) Highly Compressible:

$$SFS \longrightarrow UNSS \longrightarrow UFC \longrightarrow UFS \longrightarrow SNSS \longrightarrow SFC \longrightarrow UNUNUN \longrightarrow SNSNSN.$$

The lifetime reduces with turbulent Mach number for topologies existing in the $p = 0$ plane (UNSS, SNSS, SFS, UFC). However, for topologies existing at high dilatation levels viz. UFS, SFC, SNSNSN and UNUNUN, the lifetime first increases and later show little variation with M_t. Reynolds number seems to have a negligible influence on the lifetime of topology. Further, the lifetime of topology is found to decrease with increasing magnitude of dilatation ($|a_{ii}|$).

The authors acknowledge the computational support provided by the High-Performance Computing (HPC) Center of the Indian Institute of Technology Delhi, New Delhi, India.

REFERENCES

Ashurst, Wm. T., Chen, J-Y & Rogers, M. M. 1987*a* Pressure gradient alignment with strain rate and scalar gradient in simulated Navier–Stokes turbulence. *Phys. Fluids* **30** (10), 3293–3294.

Ashurst, Wm. T., Kerstein, A. R., Kerr, R. M. & Gibson, C. H. 1987*b* Alignment of vorticity and scalar gradient with strain rate in simulated Navier–Stokes turbulence. *Phys. Fluids* **30** (8), 2343–2353.

Atkinson, Callum, Chumakov, Sergei, Bermejo-Moreno, Ivan & Soria, Julio 2012 Lagrangian evolution of the invariants of the velocity gradient tensor in a turbulent boundary layer. *Phys. Fluids* **24** (10), 105104.

Bechlars, P. & Sandberg, R. D. 2017 Evolution of the velocity gradient tensor invariant dynamics in a turbulent boundary layer. *J. Fluid Mech.* **815**, 223242.

Bhatnagar, Akshay, Gupta, Anupam, Mitra, Dhrubaditya, Pandit, Rahul & Perlekar, Prasad 2016 How long do particles spend in vortical regions in turbulent flows? *Phys. Rev. E* **94** (5), 1–8.

Cantwell, Brian & Coles, Donald 1983 An experimental study of entrainment and transport in the turbulent near wake of a circular cylinder. *Journal of fluid mechanics* **136**, 321–374.

Cantwell, Brian J. 1992 Exact solution of a restricted Euler equation for the velocity gradient tensor. *Phys. Fluids A* **4** (4), 782–793.

Cantwell, Brian J. 1993 On the behavior of velocity gradient tensor invariants in direct numerical simulations of turbulence. *Phys. Fluids A* **5** (8), 2008–2013.

Chen, Hudong, Herring, Jackson R., Kerr, Robert M. & Kraichnan, Robert H. 1989 Non-Gaussian statistics in isotropic turbulence. *Phys. Fluids A* **1** (11), 1844–1854.

Chevillard, Laurent & Meneveau, Charles 2006 Lagrangian dynamics and statistical geometric structure of turbulence. *Phys. Rev. Lett.* **97** (17), 174501.

Chevillard, Laurent & Meneveau, Charles 2011 Lagrangian time correlations of vorticity alignments in isotropic turbulence: Observations and model predictions. *Phys. Fluids* **23** (10), 101704.

Chong, M. S., Perry, A. E. & Cantwell, B. J. 1990 A general classification of three-dimensional flow fields. *Phys. Fluids A* **2** (5), 765–777.

Chu, You-Biao & Lu, Xi-Yun 2013 Topological evolution in compressible turbulent boundary layers. *J. Fluid Mech.* **733**, 414–438.

Danish, Mohammad, Sinha, Sawan Suman & Srinivasan, Balaji 2016*a* Influence of compressibility on the lagrangian statistics of vorticity–strain-rate interactions. *Phys. Rev. E* **94** (1), 013101.

Danish, Mohammad, Suman, Sawan & Girimaji, Sharath S 2016*b* Influence of flow topology and dilatation on scalar mixing in compressible turbulence. *J. Fluid Mech.* **793**, 633–655.

Danish, Mohammad, Suman, Sawan & Srinivasan, Balaji 2014 A direct numerical simulation-based investigation and modeling of pressure Hessian effects on compressible velocity gradient dynamics. *Phys. Fluids* **26** (12), 126103.

Elghobashi, S. & Truesdell, G. C. 1992 Direct simulation of particle dispersion in a decaying isotropic turbulence. *J. Fluid Mech.* **242**, 655700.

Girimaji, S.S. 1991 Assumed β-pdf Model for Turbulent Mixing: Validation and Extension to Multiple Scalar Mixing. *Combustion Science and Technology* **78** (4-6), 177–196.

Girimaji, Sharath S. & Speziale, Charles G. 1995 A modified restricted Euler equation for turbulent flows with mean velocity gradients. *Phys. Fluids* **7** (6), 1438–1446.

Jeong, Eunhwan & Girimaji, Sharath S. 2003 Velocity-gradient dynamics in turbulence: Effect of viscosity and forcing. *Theor. Comp. Fluid Dyn.* **16** (6), 421–432.

Kerimo, Johannes & Girimaji, Sharath S. 2007 Boltzmann–BGK approach to simulating weakly compressible 3D turbulence: comparison between lattice Boltzmann and gas kinetic methods. *J. Turbul.* **8** (46), 1–16.

Kumar, G., Girimaji, Sharath S. & Kerimo, J. 2013 WENO-enhanced gas-kinetic scheme for direct simulations of compressible transition and turbulence. *J. Comput. Phys.* **234**, 499–523.

Liao, Wei, Peng, Yan & Luo, Li-Shi 2009 Gas-kinetic schemes for direct numerical simulations of compressible homogeneous turbulence. *Phys. Rev. E* **80** (4), 046702.

Lozano-Durán, Adrián, Holzner, Markus & Jiménez, Javier 2015 Numerically accurate computation of the conditional trajectories of the topological invariants in turbulent flows. *Journal of Computational Physics* **295**, 805–814.

Lüthi, Beat, Tsinober, Arkady & Kinzelbach, Wolfgang 2005 Lagrangian measurement of vorticity dynamics in turbulent flow. *J. Fluid Mech.* **528**, 87–118.

Martín, Jesús, Ooi, Andrew, Chong, M.S. & Soria, Julio 1998 Dynamics of the velocity gradient tensor invariants in isotropic turbulence. *Phys. Fluids* **10**, 2336–2346.

Martín, M Pino, Taylor, Ellen M, Wu, Minwei & Weirs, V Gregory 2006 A bandwidth-optimized WENO scheme for the effective direct numerical simulation of compressible turbulence. *J. Comput. Phys.* **220** (1), 270–289.

Meneveau, Charles 2011 Lagrangian dynamics and models of the velocity gradient tensor in turbulent flows. *Annu. Rev. Fluid Mech.* **43**, 219–245.

Ohkitani, Koji 1993 Eigenvalue problems in three-dimensional Euler flows. *Phys. Fluids A* **5** (10), 2570–2572.

O'Neill, Philippa & Soria, Julio 2005 The relationship between the topological structures in turbulent flow and the distribution of a passive scalar with an imposed mean gradient. *Fluid Dyn. Res.* **36** (3), 107–120.

Ooi, Andrew, Martin, Jesus, Soria, Julio & Chong, M.S. 1999 A study of the evolution and characteristics of the invariants of the velocity-gradient tensor in isotropic turbulence. *J. Fluid Mech.* **381**, 141–174.

Parashar, N., Sinha, S. S., Danish, M. & Srinivasan, B. 2017*a* Lagrangian investigations of vorticity dynamics in compressible turbulence. *Physics of Fluids* **29** (10), 105110.

Parashar, N., Sinha, S. S., Srinivasan, B. & Manish, A. 2017*b* Gpu-accelerated direct numerical simulations of decaying compressible turbulence employing a gkm-based solver. *Int. J. Numer. Meth. Fluids* **83** (10), 737–754.

Pirozzoli, S. & Grasso, F. 2004 Direct numerical simulations of isotropic compressible turbulence: influence of compressibility on dynamics and structures. *Phys. Fluids* **16** (12), 4386–4407.

Pope, Stephen B. 2002 Stochastic Lagrangian models of velocity in homogeneous turbulent shear flow. *Phys. Fluids* **14** (5), 1696–1702.

Pumir, Alain 1994 A numerical study of the mixing of a passive scalar in three dimensions in the presence of a mean gradient. *Phys. Fluids* **6** (6), 2118–2132.

Samtaney, Ravi, Pullin, Dale I. & Kosovic, Branko 2001 Direct numerical simulation of decaying compressible turbulence and shocklet statistics. *Phys. Fluids* **13** (5), 1415–1430.

da Silva, Carlos B. & Pereira, José C.F. 2008 Invariants of the velocity-gradient, rate-of-strain, and rate-of-rotation tensors across the turbulent/nonturbulent interface in jets. *Phys. Fluids* **20** (5), 55101–55101.

Soria, J., Sondergaard, R., Cantwell, B. J., Chong, M. S. & Perry, A. E. 1994 A study of the fine-scale motions of incompressible time-developing mixing layers. *Phys. Fluids* **6** (2), 871–884.

Suman, S. & Girimaji, S. S. 2009 Homogenized Euler equation: a model for compressible velocity gradient dynamics. *J. Fluid Mech.* **620**, 177–194.

Suman, Sawan & Girimaji, Sharath S. 2010*a* On the invariance of compressible Navier–Stokes and energy equations subject to density-weighted filtering. *Flow Turbul. Combust.* **85** (3-4), 383–396.

Suman, Sawan & Girimaji, Sharath S. 2010*b* Velocity gradient invariants and local flow-field topology in compressible turbulence. *J. Turbul.* **11** (2), 1–24.

Suman, Sawan & Girimaji, Sharath S. 2012 Velocity-gradient dynamics in compressible turbulence: influence of Mach number and dilatation rate. *J. Turbul.* **13** (8), 1–23.

Vieillefosse, P. 1982 Local interaction between vorticity and shear in a perfect incompressible fluid. *J. Phys.* **43** (6), 837–842.

Xu, Haitao, Pumir, Alain & Bodenschatz, Eberhard 2011 The pirouette effect in turbulent flows. *Nature Phys.* **7** (9), 709–712.

Xu, K., KIM, CHONGAM, MARTINELLI, LUIGI & JAMESON, ANTONY 1996 BGK-based schemes for the simulation of compressible flow. *Int. J. Comput. Fluid D.* **7** (3), 213–235.

Yeung, P. K. & Pope, S. B. 1988 An algorithm for tracking fluid particles in numerical simulations of homogeneous turbulence. *J. Comput. Phys.* **79** (2), 373–416.

Yeung, P. K. & Pope, S. B. 1989 Lagrangian statistics from direct numerical simulations of isotropic turbulence. *J. Fluid Mech.* **207**, 531–586.